93

JAN 26 2001
LIBRARY

ISSN 1343-2230

CNS-REP-28
December, 2000

CNS

CNS Report

CNS-REP-28

Study of Double-Lambda Hypernuclei by Using Cylindrical Detector System

J. P. Nakano

Center for Nuclear Study, Graduate School of Science, the University of Tokyo
7-3-1, Hongo, Bunkyo-ku, Tokyo, 113-0033, Japan

Fermilab Library
0 1160 0089422 4

Center for Nuclear Study(CNS)

Graduate School of Science, the University of Tokyo
7-3-1, Hongo, Bunkyo-ku, Tokyo, 113-0033, Japan
Correspondence: cnsoffice@cns.s.u-tokyo.ac.jp

Study of Double-Lambda Hypernuclei by Using Cylindrical Detector System

Doctor of Science

Joe P. Nakano
Department of Physics, University of Tokyo

June 23, 2000

Abstract

I constructed a Cylindrical Detector System(CDS) for the study of S=-2 nuclear system, and carried out BNL-AGS-E906 experiment at the D-line of the AGS accelerator in Brookhaven National Laboratory. The title of E906 experiment was 'Experiment to Detect Double-Lambda Hypernuclei by Observing Characteristic Pi-Mesonic Decay'.

The CDS was optimized to detect π^-'s from weak decay of hypernuclei whose momentum were comparably low; 90$\sim$140(MeV/c). The momentum resolution was finally achieved to be 8.2MeV/c(FWHM) for 100MeV/c.

During a run in 1998, 1.1×10^5 (K^-, K^+)reaction was identified among $0.9\text{x}10^{12}$ K^-incident, and a number of sequential π^-decays from S=-2 nuclear system were detected by CDS. Among them, the sequential decay mode of a double-lambda hypernucleus, ${}^{4}_{\Lambda\Lambda}\text{H} \rightarrow {}^{4}_{\Lambda}\text{He} + \pi^-$, ${}^{4}_{\Lambda}\text{He} \rightarrow {}^{3}\text{He} + \text{p} + \pi^-$ was identified. The momentum of π^- from ${}^{4}_{\Lambda\Lambda}\text{H} \rightarrow {}^{4}_{\Lambda}\text{He} + \pi^-$ is measured to be 116.4$\pm$1.4(stat.)$\pm$1.2(syst.)(MeV/c). Asuuming that the ${}^{4}_{\Lambda\Lambda}\text{H}$ mainly decays into an excited state of ${}^{4}_{\Lambda}\text{He}^*$(Ex=1.15(MeV)), this gives a ${}^{4}_{\Lambda\Lambda}\text{H}$ mass of 4106.2 $\pm$0.94(stat.)$\pm$0.80(syst.)(MeV), which corresponds to a $\Lambda\Lambda$ bond energy $\Delta B_{\Lambda\Lambda}$of 0.47 $\pm$0.94(stat.)$\pm$0.80(syst.)(MeV).

Contents

Chapter 1

Introduction

A hypernucleus is a nucleus in which constituent nucleons are replaced by hyperons (Λ,Σ or Ξ). Until now, about 30 hypernuclear species of single strangeness system (S=-1) have been discovered and their properties have been studied by a series of experiments. Theoretical attempts to explain the S=-1 system in a unifying way with NN system have been considerably successful. Through those studies we can also get information on the interaction between hyperon and nucleon (YN).

On the other hand, we have few experimental data about the system containing two strange quarks; the strangeness -2 (S=-2) system. It's mainly due to the difficulty of production of such a system, so that higher statistics were not expected. It is rather difficult to obtain detailed information of $\Lambda\Lambda$ interaction from these experimental data, even though it is crucial to study Λ-Λ, Ξ-nucleon interaction experimentally for understanding the baryon-baryon interaction extended to S=-2 system in a unified way. Furthermore, the study of the system is an important step to understanding multi-strangeness systems, S=-3, -4,...., multi-strange nuclei, as well as strange quark matter which is expected in QCD.

It is certainly necessary to study the S=-2 system with higher statistics than ever, so we proposed a unique way for the spectroscopy of S=-2 system using the Cylindrical Detector System (CDS) and a high intensity K^- beam at AGS. Our proposal was approved as E906 at AGS Accelerator of Brookhaven National Laboratory (BNL-AGS-E906), whose title is "Experiment to Detect Double Lambda Hypernuclei by Observing Characteristic pi-Mesonic Decay". The main purpose of this experiment is to determine the mass of double-lambda hypernuclei with high statistics by measuring the momentum of sequentially decaying pions via weak interaction. We can get high intensity K^-beam in the D-line experimental hall at the AGS, and abundant $\Lambda\Lambda$ hypernuclei are expected to be produced in the large amount of (K^-, K^+) reaction on a target nucleus followed by $\Lambda\Lambda$ conversion processes.

In the following section, I briefly review the study of S=-2 system and summarize production process and decay of $\Lambda\Lambda$ hypernuclei. In the last section, I will explain the principle of our experiment.

1.1 Strangeness=-2 system

One of the most intriguing predictions for S=-2 objects is an H-particle. R.L. Jaffe predicted a possibility of flavor-singlet stable state 'H-dibaryon' consisting of 6-quark ($uuddss$) with mass smaller than $2M_\Lambda$ by 80 MeV[1]. Such a strange quark system originates from the color magnetic interaction of QCD. Many calculations followed with a variety of predicted masses [2][3][4][5][6].

Many experiments to search for a bound H-particle directly have been carried out so far. There is no conclusive evidence, but they can eliminate the possibility of such a tightly-bound H-particle predicted by Jaffe. KEK-E224 group recently published a report suggesting an H-dibaryon resonance state, that is, enhanced production of $\Lambda\Lambda$ pairs near 2 Λ mass threshold [7]. They claimed that the data was not reproduced well by any theoretical predictions without Λ-Λ interaction, but it's hard to get more information due to their limited statistics.

On the other hand, a $\Lambda\Lambda$ hypernucleus, containing Λ-Λ ($uds - uds$), has the same quantum number as H-particle. If we know the mass of $\Lambda\Lambda$ hypernuclei, we can extract the information on Λ-Λ interaction. This is the most feasible way to measure the magnitude of the Λ-Λ interaction.

Moreover, the existence of $\Lambda\Lambda$ hypernuclei can limit the region of the mass of H-particle. If the mass of H-particle, M_H, is far lighter than $2M_\Lambda$, $\Lambda\Lambda$ in nuclei decays into H-dibaryon through strong interaction, and $\Lambda\Lambda$ hypernuclei will not be observed. To the contrary, if M_H is heavier than $2M_\Lambda$, H-dibaryons can decay to $\Lambda\Lambda$ hypernuclei. If we detect $\Lambda\Lambda$ hypernucleus and measure the mass of its nucleus, we can deduce lower limit of M_H,

$$M_H > 2M_\Lambda - B_{\Lambda\Lambda}$$

where $B_{\Lambda\Lambda}$is the binding energy of $\Lambda\Lambda$ inside the nucleus.

Historically, only three observations of $\Lambda\Lambda$ hypernuclei have been reported in emulsion experiments.

Table 1.1: Species of $\Lambda\Lambda$ hypernuclei and the magnitude of interaction between Λ-Λ inside the nucleus, $\Delta B_{\Lambda\Lambda}$.

	$\Delta B_{\Lambda\Lambda}$ (MeV)	References
${}^{10}_{\Lambda\Lambda}$Be	4.3 ± 0.4	M.Danysz [8]
${}^{6}_{\Lambda\Lambda}$He	4.7 ± 0.5	D.J.Prowse [9]
${}^{10}_{\Lambda\Lambda}$Be	-4.9 ± 0.7	
or ${}^{13}_{\Lambda\Lambda}$B	4.9 ± 0.7	S.Aoki[10]

Table 1.1 shows species of the observed $\Lambda\Lambda$ hypernuclei and the magnitude of interaction between $\Lambda\Lambda$ inside the nucleus, $\Delta B_{\Lambda\Lambda}$. $\Delta B_{\Lambda\Lambda}$ is calculated to be the difference between the mass of ${}^{A}_{\Lambda\Lambda}Z$ and the mass of ${}^{A-1}_{\Lambda}Z + \Lambda$.

Danynsz's data is the first reported event in 1963. This emulsion plate was processed again later by Fowler et al., and the result reported in his thesis was published by Dalitz et al. [11]. $\Delta B_{\Lambda\Lambda}$ value in Table 1.1 is the one from this paper.

In ref [9], it was reported that a ${}^{6}_{\Lambda\Lambda}$He event was discovered in emulsion stack behind the Ω^- bubble chamber at Brookhaven National Laboratory. The ${}^{6}_{\Lambda\Lambda}$He system, named as 'lambpha' by Bando et al [12], is very important, because this nucleus is the lightest triple-closed shell analogous to α, and it is expected to be a cluster unit in multi-strangeness systems. However, only a schematic drawing of the star event was presented on this letter by Prowse and other necessary data were not, so that it gives no confirmatory evidence. In ref [11], they examined consistency between these two events; they checked whether the two $\Delta B_{\Lambda\Lambda}$ values can be accounted for by the same $V_{\Lambda\Lambda}(r)$ potential. There are no reasonable potentials that allow them to be compatible.

The third event was discovered at KEK-E176 experiment (a hybrid-emulsion method). It was published by S.Aoki et al. [10]. This event has been interpreted as two kinds of candidate, ${}^{10}_{\Lambda\Lambda}$Be or ${}^{13}_{\Lambda\Lambda}$B, because the second decay of the single-Λ hypernucleus was a non-mesonic decay and therefore the unique assignment of the species was not made. The sign of $\Delta B_{\Lambda\Lambda}$ depends on the species.

It is very frustrating that these data are insufficient or inconsistent with each other. Under such a circumstance, theorists are also arguing about the sign of interaction between Λ's. We have several theoretical models treating the baryon-baryon interaction with meson exchange. Models that are successful in fitting NN+YN will not necessarily be able to describe the Λ-Λ interaction. Only a model among the OBE models, so-called Nijmegen model F, predicts the sign to be attractive.

We have also little information on Ξ^- hypernuclei. The potential well depth was claimed to be 24 MeV based on the emulsion experiments in 1960's [13], however these data have not necessarily interpreted as an evidence of Ξ^- hypernuclei. An experiment KEK-E224 tried to produce Ξ^- hypernuclei in the (K^-, K^+) reaction on ${}^{12}C$ target, but did not show a clear peak due to low statistics. Nevertheless, the missing mass spectrum around the threshold region of quasi-free production of Ξ^- was compared with a theoretical calculation and a conclusive remark that the potential well depth should be less than 20 MeV [14][15]. A similar conclusion has been made based on an experiment AGS-E885 in the (K^-, K^+) reaction on ${}^{12}C$ target [16].

1.2 Double-lambda hypernuclei

1.2.1 Production of double-lambda hypernuclei

Production process of $\Lambda\Lambda$ can be written as a two step reaction.

$$K^- + p \longrightarrow K^+ + \Xi^-$$

$$\Xi^- + p \longrightarrow \Lambda\Lambda + Q(28\mathrm{MeV})$$

After Ξ^- is produced from (K^-, K^+) reaction as a doorway to S=-2 production, there may be two mechanisms to produce $\Lambda\Lambda$ hypernuclei, which is shown in Fig 1.1.

- Stop Ξ^-process
- Direct process

In the stopped Ξ process, quasi-free Ξ^-'s are emitted in the (K^-, K^+) reaction and brought to rest by ionization loss in the target material. After Ξ^--atom is formed, the $\Xi^-$is eventually absorbed by the nucleus. Ξ^-in the nucleus will be converted into $\Lambda\Lambda$ via strong interaction, $\Xi^-p \rightarrow \Lambda\Lambda$.

In spite of its Q value (28 MeV), absorbed Ξ^-'s form $\Lambda\Lambda$ fragment with a relatively large probability. In Table 1.2.1, KEK-E176 scanned events are classified. In this experiment, an emulsion stack sandwiched between silicon micro-strip detectors was exposed in a 1.66 GeV/c separated K^- beam.

Table 1.2: Classification of KEK-E176 scanning data

	Total number	S=-2		S=-1	
Capture in light nuclei	31	DH	1	SH	8
		TH	2	VR	8
		DH or TH	1		
Capture in heavy nuclei	47	VR2	≤ 3	VR	18
Direct process $P_{K+} \geq$1.0GeV/c	240		2(?)		1
Direct process P_{K+} <1.0GeV/c	1400		3		70

DH : double-Λ hypernuclei
TH : twin hyperfragment
SH : single-Λ hypernuclei
VR : events with total visible energy release > 28MeV
VR2: events with total visible energy release $\geq$160 MeV

In the direct process, only light fragments can be identified.

In the specific cases the $\Lambda\Lambda$ compound state is formed with a "sticking" probability of more than 10%. The Ξ^-emission probability is about 70~80% of the total quasi-free events and about 0.3% of the quasi-free events will be converted to a $\Lambda\Lambda$ compound state with a typical stopping probability of Ξ^- in the target of 3% [17].

On the other hand, the remaining 20~30% of the quasi-free Ξ^-production will be followed by the secondary reaction of a Ξ^-inside the same nucleus, such as

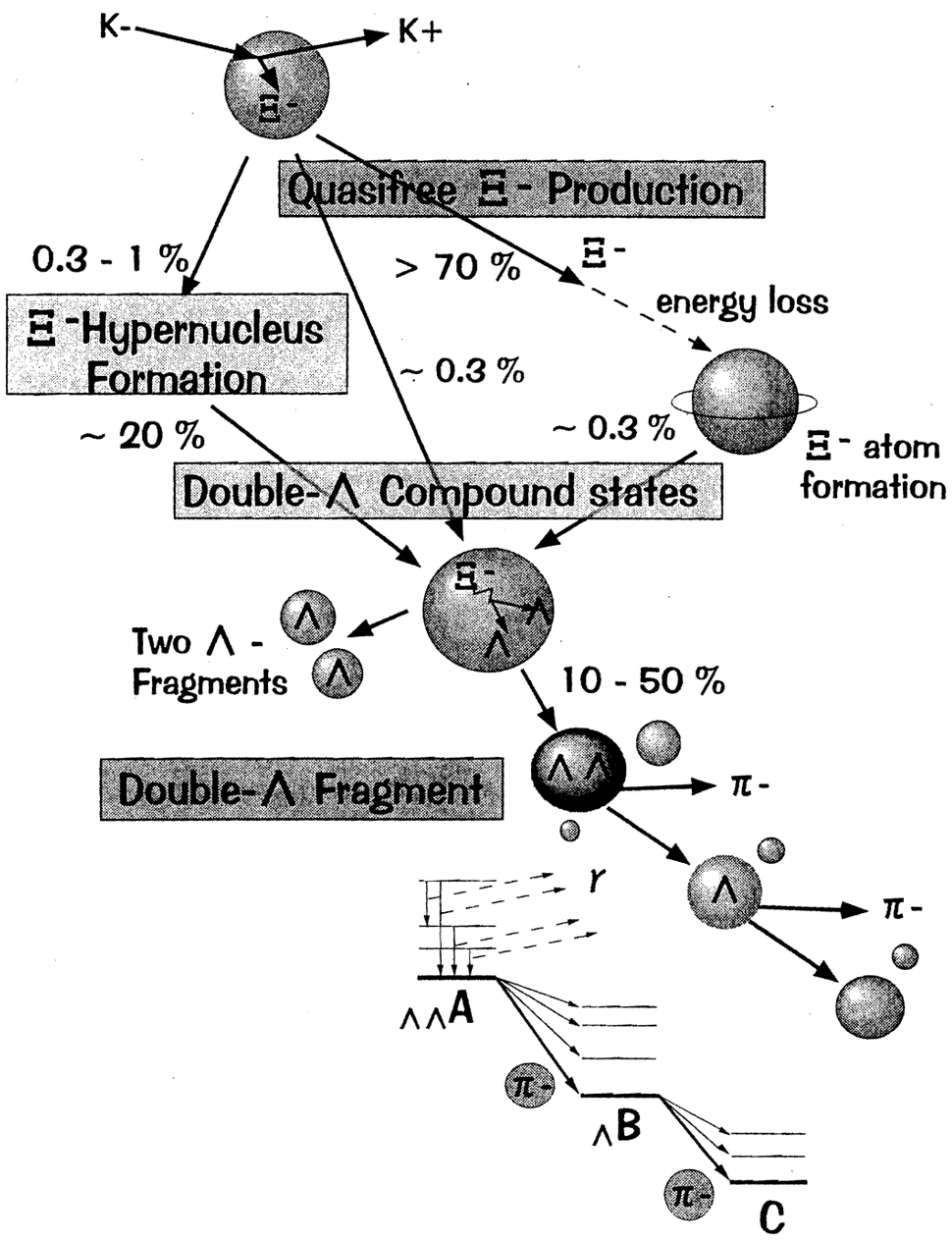

Figure 1.1: Double-lambda hypernuclear production process

$\Xi^- p \rightarrow \Lambda\Lambda$. In this case two Λ's may have a chance of being trapped, leading to a $\Lambda\Lambda$ hypernucleus production which is the so-called direct process. A theoretical attempt[18] to estimate the production rate of the $\Lambda\Lambda$ compound nucleus via such a process gives about 0.3% per quasi-free reaction for a ^{12}C target. This assumed a Ξ-nucleus potential depth of 15 MeV. The (K^-, K^+) reaction may also directly produce Ξ^-nuclear state , if any, and the Ξ^- nuclear state will be converted into a $\Lambda\Lambda$ hypernuclear state with some probability.

In any case, the $\Lambda\Lambda$ compound nucleus will subsequently decay into hyperfragments containing one or two hyperons per fragment, for example ${}^{6}_{\Lambda\Lambda}$He and ${}^{4}_{\Lambda\Lambda}$H (Fig 1.1).

1.2.2 Decay of double lambda hypernuclei

A Λ hypernucleus decays via weak interaction. The decay mechanism is classfied into two; one is "mesonic decay", decaying with pi meson emission, the other is "nonmesonic decay" without pi meson emission. Because of the Pauli suppression due to the small momentum available to the nucleon, the mesonic decay is dominated by the nonmesonic one, in particular, for heavy nuclei. Nevertheless the probability of mesonic decay of light hypernuclei is larger, so that the probability of $\Lambda\Lambda$ hypernuclei decaying with sequential emission of two π mesons is expected to be considerably large.

In the decay of light hypernuclei, three-body decay spectra generally predominate. Fig 1.2 shows the observed π^-decay spectrum of ${}^{4}_{\Lambda}$He three-body decay taken in the experiment compared with a theoretical π^-spectrum $\Gamma_{\pi^-}({}^{4}_{\Lambda}\mathrm{He})/\Gamma_\Lambda$ [19]. They took into account the final-state nuclear interaction and the pion distortion in order to realistically calculate the pionic decay to the continuum. These calculations have been successfully applied to describe the decay of ${}^{4}_{\Lambda}$H, ${}^{5}_{\Lambda}$He and so on.

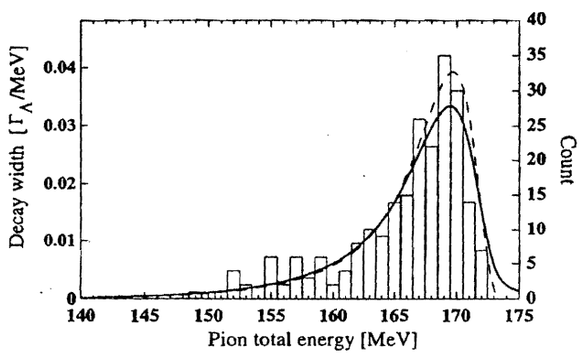

Figure 1.2: The observed π^-decay spectrum of ${}^{4}_{\Lambda}$He three-body decay taken in the emulsion experiment compared with a theoretical π^- spectrum of $\Gamma_{\pi^-}({}^{4}_{\Lambda}\mathrm{He})/\Gamma_\Lambda$[19]. The dashed line is the spectra without smearing and the bold line is the one with 1.0 MeV smearing in Lorentzian weight.

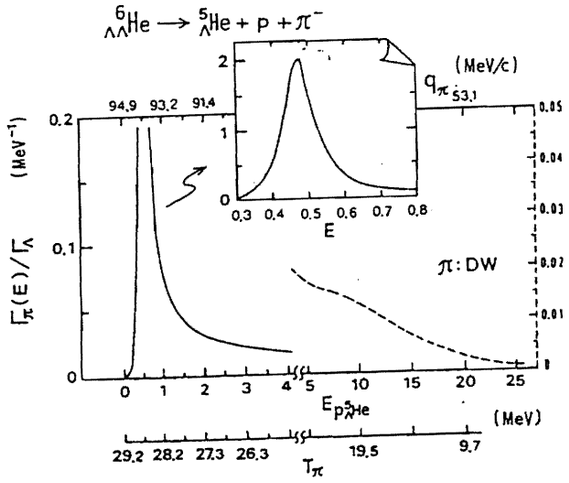

Figure 1.3: A theoretical π^- spectrum of $\Gamma_{\pi^-}(^{6}_{\Lambda\Lambda}\mathrm{He})/\Gamma_{\Lambda}$

In the case of $\Lambda\Lambda$ hypernuclei, the situation may be the same as in Λ hypernuclei case; for example, $^{6}_{\Lambda\Lambda}$He will only decay into a 3-body final state. Fig 1.3 shows an expected π^- spectrum of $^{6}_{\Lambda\Lambda}$He by a similar treatment [20], which produces an almost monoenergetic pion spectrum (about 100 MeV/c with 1.7 Mev/c FWHM).

Even if the hypernuclei would decay into three-body, we can identify the species of decaying nuclei by observing π^-momentum. The production of $\Lambda\Lambda$ hypernucleus and its mass can be measured by two pions coming from sequential mesonic weak decays.

1.3 Experimental principle of E906

The experimental method for identifying $\Lambda\Lambda$ hypernuclei is based on the observation of the sequential decaying charged π^- from $\Lambda\Lambda$ hypernuclei in coincidence with the decaying π^- from single-Λ hypernuclei which are well known.

One of the characteristics of our experiment is that the $\Lambda\Lambda$ hypernuclei can be identified only by measuring the momentum of 2 π^-'s without investigating the reaction vertex precisely as is done in the emulsion experiment. Momentum of π^- gives information about species of hypernuclei. This method will lead to a new spectroscopy of double-Λ hypernuclei by using high intensity kaons in the future.

For example, I explain the case of $^{4}_{\Lambda\Lambda}$H.

$^{4}_{\Lambda\Lambda}$H will decay as follows:

$$^{4}_{\Lambda\Lambda}\mathrm{H} \longrightarrow {}^{4}_{\Lambda}\mathrm{He} + \pi^- \longrightarrow {}^{3}_{\Lambda}\mathrm{H} + \mathrm{p} + \pi^-$$
$$\hookrightarrow \mathrm{He}^3 + \mathrm{p} + \pi^- \qquad\qquad \hookrightarrow \mathrm{He}^3 + \pi^-$$

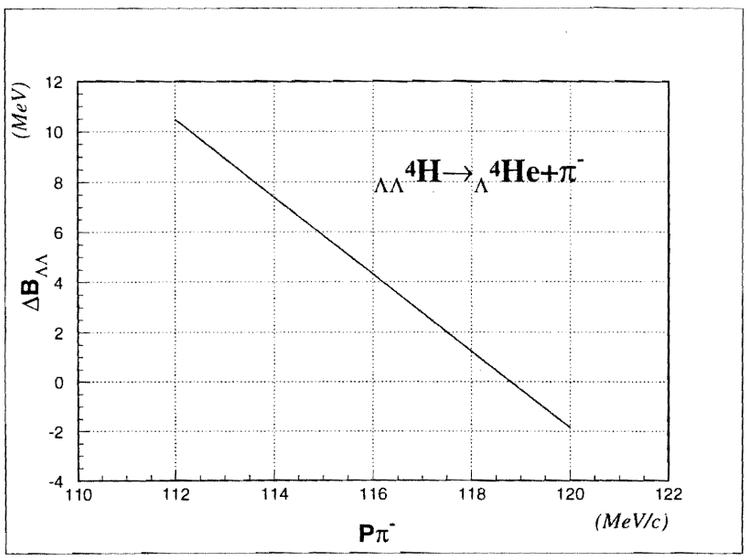

Figure 1.4: The ΛΛ bond energy $\Delta B_{\Lambda\Lambda}$ is plotted as a function of the weak decay pion momentum p_π from ${}^{4}_{\Lambda\Lambda}H$ decay to the ground state of ${}^{4}_{\Lambda}He$.

The momentum of π^- from ${}^{3}_{\Lambda}H$ is 114.3 (MeV/c). As Fig 1.2 shows, π^- from ${}^{4}_{\Lambda}He$ three-body decay is well-known. Branching ratios of π^- are $\sim 0.34\Gamma_\Lambda$ and $\sim 0.30\Gamma_\Lambda$ for ${}^{3}_{\Lambda}H$ and ${}^{4}_{\Lambda}He$, respectively. If we measure another pion momentum in coincidence with the pion from single Λ hypernuclei decay, we can obtain the mass of double-lambda hypernuclei. Fig 1.4 shows the relation between $\Delta B_{\Lambda\Lambda}$ and decaying π^-momentum to two-body final state. Calculated branching ratios of π^- decay rates are large enough to be observed; $\sim 0.25\Gamma_\Lambda$ and $\sim 0.52\Gamma_\Lambda$ for two-body and three-body decay of ${}^{4}_{\Lambda\Lambda}H$, respectively.

We used a ${}^{9}Be$ target for E906 because the possible ΛΛ compound nucleus has $Z \leq 3$ and the available species of the final hyperfragment are limited. Furthermore it is well known that ${}^{9}Be$ can be considered as two alphas plus a loosely bound neutron, so that the Q value for ΛΛ conversion process might be consumed in alpha particle breakup, leading to a high sticking probability for the ΛΛ pair [21]. ${}^{4}_{\Lambda\Lambda}H$ is one of possible candidates in our experiment.

A theoretical calculation, assuming the direct production process, shows that the production rate of ${}^{5}_{\Lambda\Lambda}H$ in ${}^{9}Be$ target is extreamely large [18]. According to this suggestion, we also expected to detect ${}^{5}_{\Lambda\Lambda}H$. The momentum of π^- from ${}^{5}_{\Lambda\Lambda}H$ is predicted to be around 134 MeV/c, and ${}^{5}_{\Lambda}He$, which is the daughter nucleus of ${}^{5}_{\Lambda\Lambda}H$, undergoes 3-body decay, giving a π^- momentum about 98 MeV/c.

Fig 1.5 shows an experimental result and a theoretical calculation of the π^- momentum from ${}^{5}_{\Lambda}He$. The expected momentum of ${}^{5}_{\Lambda\Lambda}H$, 134 MeV/c, is far from the π^- from other hypernuclei except for ${}^{4}_{\Lambda}H$.

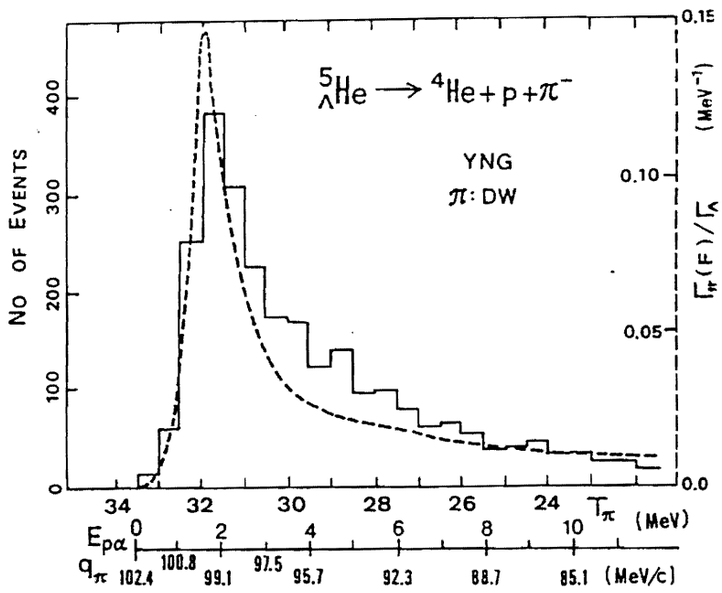

Figure 1.5: The observed π^- decay spectrum of $^{5}_{\Lambda}$He three-body decay take in the emulsion experiment and the dotted line shows a theoretical calculation [20].

Our proposal was approved and the CDS construction was started in 1995, the experiment was carried out starting 1997. We took the data for the production mainly in 1998. Details of the cylindrical detector system, design and construction, are described in the next chapter, Chapter 2. Chapter 3 shows the experimental setup in the D-line experimental hall of BNL-AGS. The procedures for the data analysis are shown in Chapter 4, which consists of three sections. In Section 4.1, the Helical-track Reconstruction Module (HRM), which is an analysis program, is briefly explained. Then the calibrations and performance evaluations of CDS are described. Section 4.2 shows the beam line analysis; an explanation of identifying the Ξ^- production via (K^-, K^+) reaction. In the last section, Section 4.3, the evaluation of the sequential pion production of the $\Lambda\Lambda$ hypernuclei is described. In Chapter 5 a discussion of the results are presented, and in Chapter 6 the final conclusions are summarized.

Chapter 2

Cylindrical Detector System

I played a main role of the planning and constructing the cylindrical detector system(CDS). The CDS comprises four main components, a cylindrical drift chamber (CDC), a z-position chamber (CDZ), a hodoscope (CDH) and a solenoid magnet. CDS was optimized to detect decay pions whose momenta lie in the range from 90 to 140 MeV/c.

Fig 2.1 shows a schematic view of CDS.

CDC plays the role of the central chamber which traces the helical track of charged particle. CDZ also gives the Z information of the track just outside the CDC. Hodoscopes which surround the CDZ provide time-of-flight (TOF) information for the event trigger. The CDS solenoid magnet provides momentum analysis for the decay particles.

I oversaw the operation of the CDS during most of the experiment. As words cannot do justice to the difficult experience this was, I will stick to the technical description only, giving the design principle and construction in this chapter. The CDS performance; momentum resolution, analysis efficiency and so on, will be described in the chapter 4.

2.1 Design principle of CDS

The primary aim of the CDS was to provide the best possible momentum resolution for the decay pion.

As is the case with detecting low momentum particles, multiple scattering inside the central chamber is not negligible. To minimize the effects of multiple scattering, we reduce the amount of material inside of chamber. This was accomplished by using a helium-based gas mixture and aluminum field wires in the CDC.

It was also desirable to fill as many layers as possible into a limited space, because we need more sampling points for better momentum resolution and recognition efficiency of tracks. The final CDC design called for 12 layers of two different types; axial layers, in which the sense wires are arranged parallel to the CDC axis, and stereo layers, in which the sense wires are inclined with respect to the Z axis.

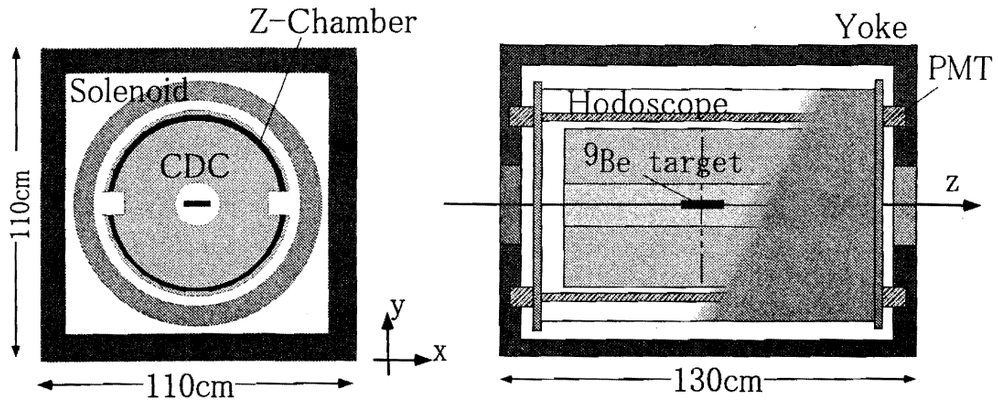

Figure 2.1: A schematic drawing of Cylindrical Detector System

The uncertainties in track momentum and direction due to multiple scattering and measurement errors are given by approximate expressions developed in [22]. These contributions to the momentum resolution are generally expressed by the following formulas.

$$\left(\frac{\delta P_T}{P_T}\right)^2 = \left(\frac{\delta P_T}{P_T}\right)_m^2 + \left(\frac{\delta P_T}{P_T}\right)_{MS}^2 \tag{2.1}$$

$$\left(\frac{\delta P_T}{P_T}\right)_m = \frac{P_T}{0.3} \cdot \frac{\sigma_{r\phi}}{L_{sample}^2 B} \cdot \sqrt{\frac{720}{N+5}} \tag{2.2}$$

$\cdots$ from number of sampling point and position resolution

$$\left(\frac{\delta P_T}{P_T}\right)_{MS} = \frac{0.05}{\beta B} \cdot \sqrt{\frac{1.43}{L_{sample} X_{rad}}} \tag{2.3}$$

$\cdots$ from Multiple scattering

where P_T is transverse momentum (GeV/c), $\sigma_{r\phi}$ is spatial resolution, L_{sample} is sampling length, N is No. of sampling points, B is magnetic field (T), X_{rad} is radiation length within sampling area.

If we assume the following parameters, P_T=100 MeV/c, σ=200 μm, L_{sample}=20 cm, N=12, B=0.5 T, X_{rad}=640 m(for gas mixture He:C_2H_6=50:50),

- $\left(\frac{\delta P_T}{P_T}\right)_m = 2.16 \times 10^{-2}$
- $\left(\frac{\delta P_T}{P_T}\right)_{MS} = 1.52 \times 10^{-2}$

These two effects are added in quadrature to give

$$\left(\frac{\delta P_T}{P_T}\right) = 2.64 \times 10^{-2} \tag{2.4}$$

Since the final momentum is obtained from p_t as $p=p_t/\cos\alpha$, where α is a dip angle , we also need a good dip angle resolution. For this purpose, we installed the Z-chamber surrounding the CDC and several super layers of stereo wires in the CDC. If CDZ resolution is 2 mm in sigma, the contribution of the dip angle resolution is less than 1.0% even at 45deg. In conclusion, from equation (2.4) I estimate that total momentum resolution is 6MeV/c (FWHM) around 100 MeV,

Secondly, as it is necessary to detect simultaneously two pions in a sequential decay, CDS must cover a large solid angle. In a cylindrical geometry, the angular acceptance is expressed as

$$\Delta\Omega = (1 - 2\theta/\pi) \times 4\pi; \theta = tan^{-1}(\frac{R_{inner}}{L_z/2}) \tag{2.5}$$

Taking account of the forward spectrometer acceptance, we have to make the total length L_z shorter than 1 m. We chose an inner radius R_{inner} of 30 cm and total length L_z of 88 cm, so that the acceptance will be larger than 60% of 4π.

Finally, since we want to simplify the tracking algorithm and $\Delta P_t/P_t \propto \Delta B/B$, the uniformity of the magnetic field must be better than 1% or the magnetic field should be measured within this accuracy. We designed the solenoid magnet to have an almost uniform field; its variation is within 0.5% in the effective area of the drift chamber.

2.2 Cylindrical drift chamber(CDC)

The momentum of a decaying π^- from hypernuclei is relatively low; the momentum region is between 90 and 140 MeV/c. To minimize the effect of multiple scattering, we select low Z material inside the chamber.

- Al-based wire for the field wire (80 μm).
- Helium:Ethane=50:50 mixture for chamber gas.

Al field wire

As field and sense wire are localized in the chamber, it is difficult to get a realistic estimate for their contribution to multiple scattering. The density of the chamber gas (He:C_2H_6=50:50) is 0.77×10^{-3} g/cm^3. The amounts of Al and W wire, averaged over the chamber volume are 0.55×10^{-3} g/cm^3 and 0.28×10^{-3} g/cm^3, respectively, which are comparable with the density of the chamber gas (Table 2.2). In this case, the contribution of the wire to multiple scattering is small.

At the beginning we intended to use pure Al wire assembled by a clipping technique, but 80 μm Al wire was so thin that the wire was broken as soon as it was clipped. Eventually, we used Au-plated Al wire assembled by soldering.

Table 2.1: Density and radiation length of materials inside of the chamber

	X_0; Radiation length$[g^{-1}/cm^2]$	ρ; Density of material$[g/cm^3]$	$\frac{X_0}{\rho}$ [m]
Al	24	0.55×10^{-3}	430
W	6.8	0.28×10^{-4}	240
He:C_2H_6=50:50	0.49	0.77×10^{-3}	640

Helium-based chamber gas

Helium has the largest radiation length of all gases except for hydrogen (Table 2.2). We use helium-based gas for drift chamber, so that we can keep the radiation length large inside the chamber.

Table 2.2: Radiation length of gases

	Radiation length $[m]$
He	5300
Ar	110
C_2H_6	340
He:C_2H_6=50:50	640
Ar:C_2H_6=50:50	82

On the other hand, there exist well known difficulties in handling He based gas for the drift chamber. The properties of gas mixtures have been well studied [23]. For Helium:Ethane=50:50 gas, the electron drift velocity is saturated and almost constant, about 4 cm/μsec over 2 kV/cm*atm (Fig 2.2). The solid curve are a calculation of Peisert and Sauli [24].

From this figure, one notices that the drift velocity changes by about 1% when the gas mixture rate changes by 1%. Its influence in spatial deviation is about 100 μm for about 1 cm drift length. In order to control the rate of gas mixture, I designed a gas flow system with a mass flow meter, whose accuracy of the flow rate is within $\pm$ 0.5%, (Fig 2.3). For stable operation of the chamber, filtering for deoxygenation and dehydration was used in order to remove impurities from the gas.

Layer design

As described in the begining of this section, we need more sampling points for a better momentum resolution and reconstruction efficiency. I tried to cram as many layers as possible into a limited space. Cylindrical chamber has 12 layers of two kinds:

- Axial Layer: sense wire is pitched parallel to Z axis, beam direction.

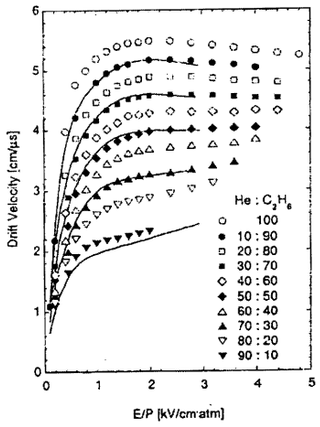

Figure 2.2: Electron drift velocity in helium and ethane mixtures

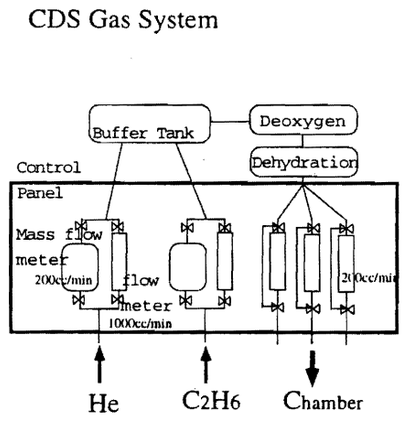

Figure 2.3: Gas Control System

- Stereo Layer: sense wire is inclined to Z axis.

Axial layer and stereo layer comprise 6 layers, respectively (Fig 2.4). Dot, circle and small dot represent the position of sense wire, field wire and shield wire, respectively. Because the stereo layer is inclined to the Z axis, we get Z information of particle tracks. CDS has two segmented groups of three stereo layers, so that we can reconstruct three dimensional information of tracks by the CDC alone.

Parameters of the wire configuration are given in Table 2.2. The overall number of cells is 576.

Table 2.3: CDC wire configuration parameter

Layer	Radius (mm)	#cells/Layer	Cell size (mm)	Stereo	Angle (degree)	HV (kV)
1	82	36	13.6	U	3.4	2.0
2	100	36	16.6	V	4.1	2.0
3	118	36	19.6	U'	4.9	2.0
4	134	36	23.4	A	0.0	2.3
5	148	36	25.8	A	0.0	2.3
6	162	36	28.2	A	0.0	2.3
7	194	60	20.2	V	4.9	2.0
8	213	60	22.0	U	5.3	2.0
9	231	60	24.0	V'	5.8	2.0
10	247	60	25.8	A	0.0	2.4
11	259	60	27.2	A	0.0	2.4
12	271	60	28.4	A	0.0	2.4

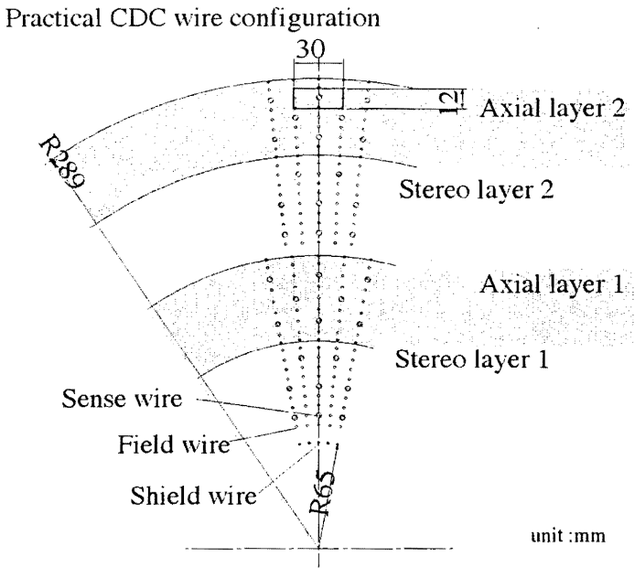

Figure 2.4: Practical CDC wire configuration

Readout

Preamplifier boards for CDC are put on the end plate, arranged like a radioactivity warning sign as shown in Fig 2.5. I design the board with 96 channels preamplifier mini cards in total, which are grouped in 6 segments consisting of 16 channels. Each sense wire is connected to a preamplifier mini card, which is so-called Radeka-Amp. Radeca-amp was originally developed in the department of instrumentation of BNL and the cards which we use for CDC are manufactured in Japan. The output from preamplifier is sent to the post-amplifier board, on which the signal is discriminated after being post-amplified. Discriminated signal is sent to the LeCroy R1877s Fastbus multi-hit TDC, which digitizes the time information as 500 psec per channel.

Structure

The size of the cylindrical chamber is 298 mm in radius and 920 mm in length. Fig 2.5 shows a schematical overview from the beam direction. Fig 2.6 shows a drawing of a side-view.

The two end plates are identical; an end plate is made of aluminum of 20 mm in thickness. A hole with radius of 50 mm is made in the center of the end-plate for incoming K^- and outgoing K^+ particles. The end-plate has about 3600 small holes into which insulator feedthroughs made of Delryn are put. The diameter of feedthrough is 4 mm, a brass tube of 1 mm in diameter is stuck into the feedthrough and the wire is assembled by soldering in the tube.

The end plates are supported by a cylindrical wall made of CFRP (Carbonized

Fiber Reinforced Plastic), 5 mm in thickness. Two posts are placed on both sides of CDC, which support the Al-end plate with the CFRP wall. The post has a channel where preamplifier boards of the Z-Chamber are put.

We use an gold-coated aluminum wire with diameter of 80 μm for the field wire and an gold coated tungsten wire with diameter of 20 μm for the sense wire.

2.3 Z chamber

We place the Z-Chamber just outside CDC in order to get additional Z information of path of particles (Fig 2.5). A conceptual design is shown in Fig 2.7. The Z-Chamber comprises one layer of MWPC with two sheets of cathode readout.

There are two identical planes, one located on the upper side and the other on the lower side of CDC (Fig 2.5). The cathode comprises 18 μm Au-Cu strips on a Kapton sheet of 35 μm in thickness. The width of the strip and the spacing between adjacent strips are 5 mm and 0.5 mm, respectively, which is shown in the Fig 2.8.

One sheet has 160 strips of 880 mm length. The cathode strips are oriented normal to the anode wire which are parallel to Z direction. The anodes are made of a gold coated tungsten wire, 30 μm thick. The pitch of the anode wires is 2.64 mm.

The chamber body consists of inner and outer FRP (Fiber Reinforced Plastic) cylinders with 920 mm long and 2 mm thick. The radii are 298 mm and 310 mm, respectively. The total gap between two cathode planes is 8 mm.

The chamber gas is Ar based gas(Ar:Ethern=50:50). An operational voltage is 2400 V.

We use the same preamplifier card as CDC's for each strip. I design the Z-Chamber preamplifier board which has 16 channels preamplifier cards. 40 preamplifier boards are installed in the channel of the CDC's posts. The output from preamplifier is sent to the post-amplifier board, RPV-022-a, which are developed by the KEK-E246 group and provided by REPIC Co. Ltd.

Instead of the twisted pair cable, a board using a logic delay IC chip was designed, which delays the signal from post-Amp board by 300 nsec. It gives a better linearity of the pulse height than the delay cable. The boards are assembled directly on the back plane of the crate for the post-Amp's. The signal amplified by post-Amp is sent to the counting house and put into the FASTBUS 1885F ADC, which analyzes the pulse height with 12 bits information.

This chamber could not be used during the physics run due to breaking down of many field wires. The difficulty with this chamber was due to the dimensional precision required for the FRP. The deformation of the frame leads to dislocation of the anode wires, and gives the wires the unexpected strains caused by electrical force. A wire was finally broken by a critical discharge.

2.4 Hodoscope

A hodoscope we called CDH surrounds the CDZ and was used for the TOF measurement and the trigger.

CDH consists of 22 logs of plastic scintillators which are made of BC-408, provided by BICRON. A log is typically assigned to cover 15 degrees in ϕ. I designed two types of logs with different dimensions; Fig 2.9 shows the two different CDH scintilalator cross section. A type is the normal type, B type, which is a little bit small, is put on both the up- and down-side of the CDC posts. Each scintillator log was 980 mm long.

It was necessary to put the PMT inside the solenoid magnet due to the limited space of the target area of the D-line. Since the PMT's were inside the magnetic field, we adopted a fine-mesh PMT (H6614) provided by Hamamatsu Photonics. Because it uses a fine-mesh dynode, fewer electrons escape due to magnetic flux, so that good gain can be maintained inside the magnetic field. The fine-mesh PMT gave sufficient gain which I expected.

The PMT's are assembled on both sides of the scintillator with a kind of light guide made of Lucite.

2.5 Solenoid magnet

Fig 2.10 shows a drawing of the solenoid magnet. It is 1180 mm wide, 1180 mm high and 1280 mm long. The radius of the inner cylinder is 356 mm. It is cooled by water. Specifications are listed in the next table.

Table 2.4: Specification of Solenoid Magnet

Maximum Magnet Flux	5	(kGauss)
Number of Turns	216	(turns/coil)
Maximum Current	2250	(A)
Voltage	73	(V)
Power Consumption	165	(KW)
Cross-section of Conductor	20 × 20 ×ϕ 8	(mm)
Resistance	28	(mΩ)
Length × Width × Height	1380 × 1180 × 1180	(mm)
Weight	7.2	(t)

We had to make some holes on the endplate in which PMT's of the hodoscope are put. In order to design the yoke, I used the computer code, named TOSCA, for calculating the magnetic field. By changing the shape of the return yoke and hole, I investigated the change of the magnetic field. I found a shape of the return yoke and the hole, which satisfies the homogeneity of 1% in the CDC volume. A typical result of the calculation is shown in Fig 2.11.

I measured the field strength all over the magnet volume with an NMR probe. The contour plot of the measured magnetic field is shown in Fig 2.12. Comparing Fig 2.12 with Fig 2.11, both profiles are quite similar.

Actually, the magnet's homogeneity is better than the calculation. For example, Fig 2.13 shows a variation rate along the line (0,0,z); z from 0 cm to 45 cm in 5 cm step, normalized to the value of the center of the magnet; (0,0,0). Its variation is within 0.5%.

Fig 2.14 shows an excitation curve, i.e. magnetic flux vs. supplied current.

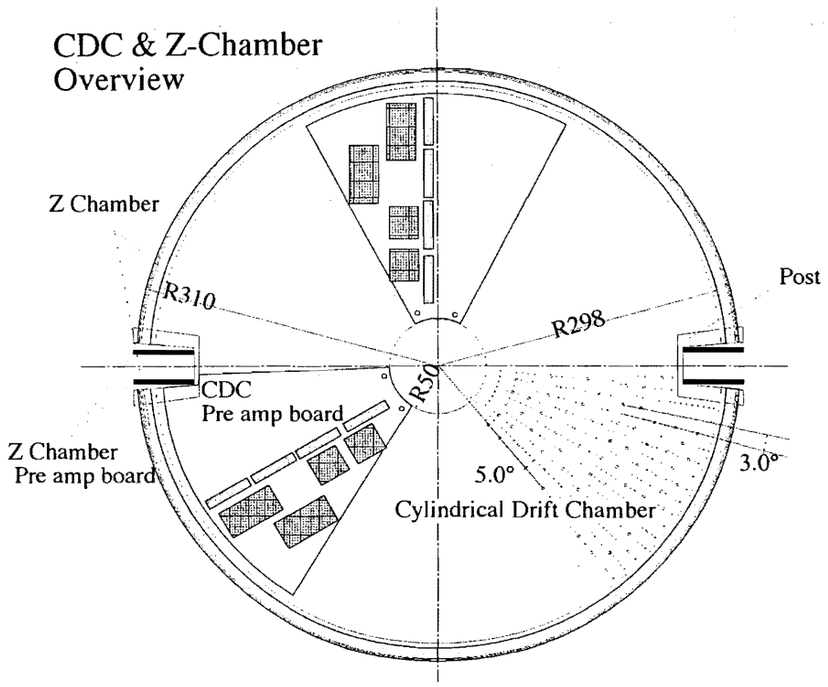

Figure 2.5: A schematical overview of the CDC & Z-chamber (the front view)

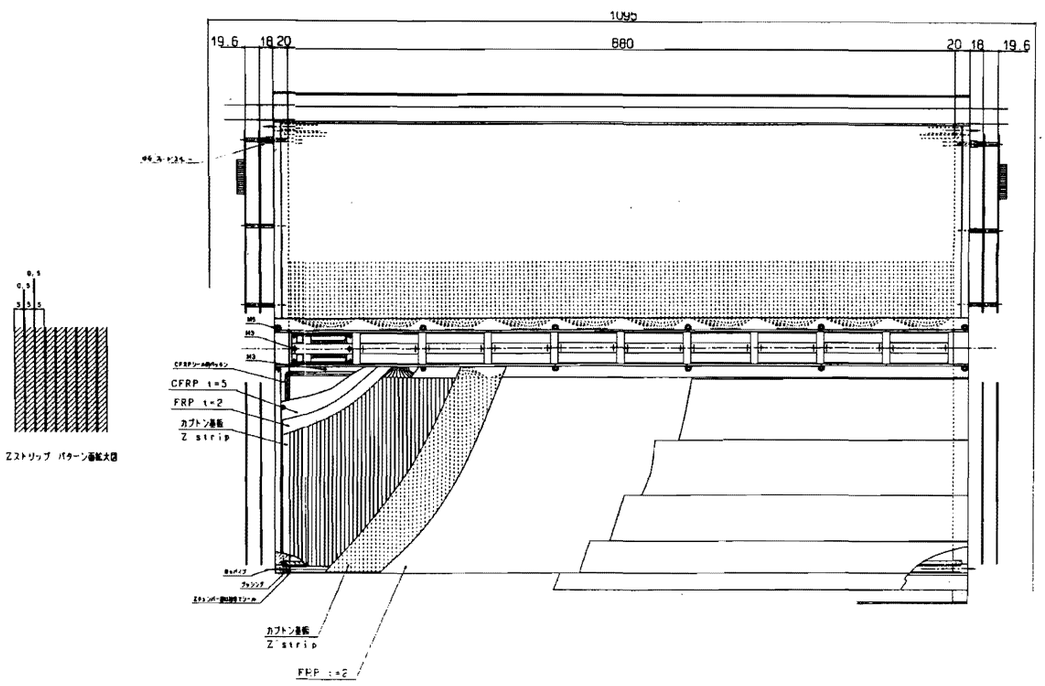

Figure 2.6: A drawing of the CDC & Z-chamber (the side view)

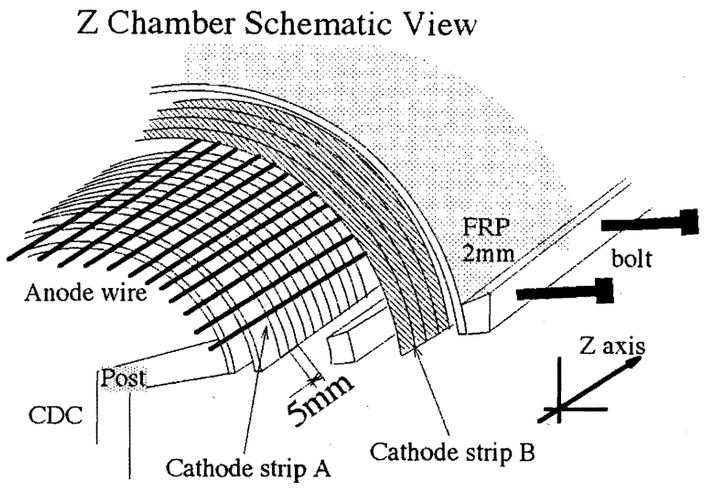

Figure 2.7: A conceptual drawing of Z chamber

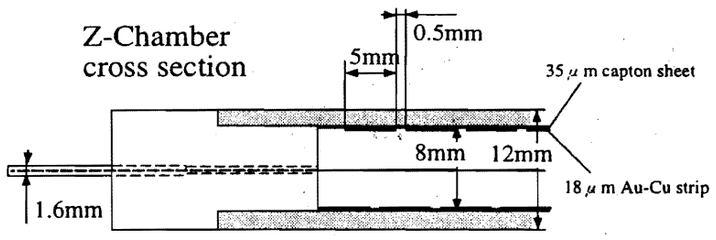

Figure 2.8: A schematic drawing of the Z-chamber

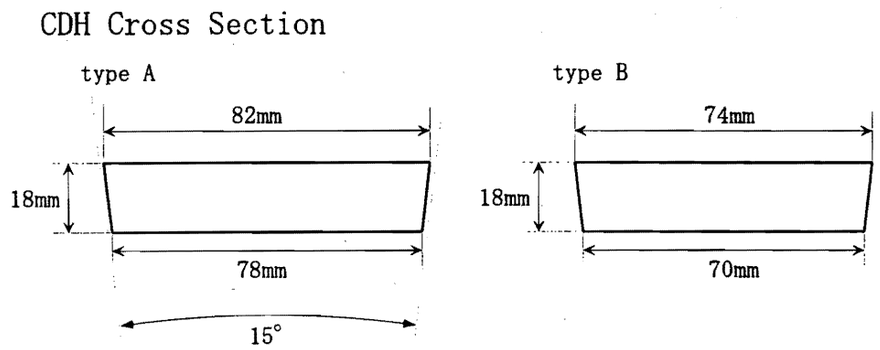

Figure 2.9: Drawings of cross section of the CDH scintillator

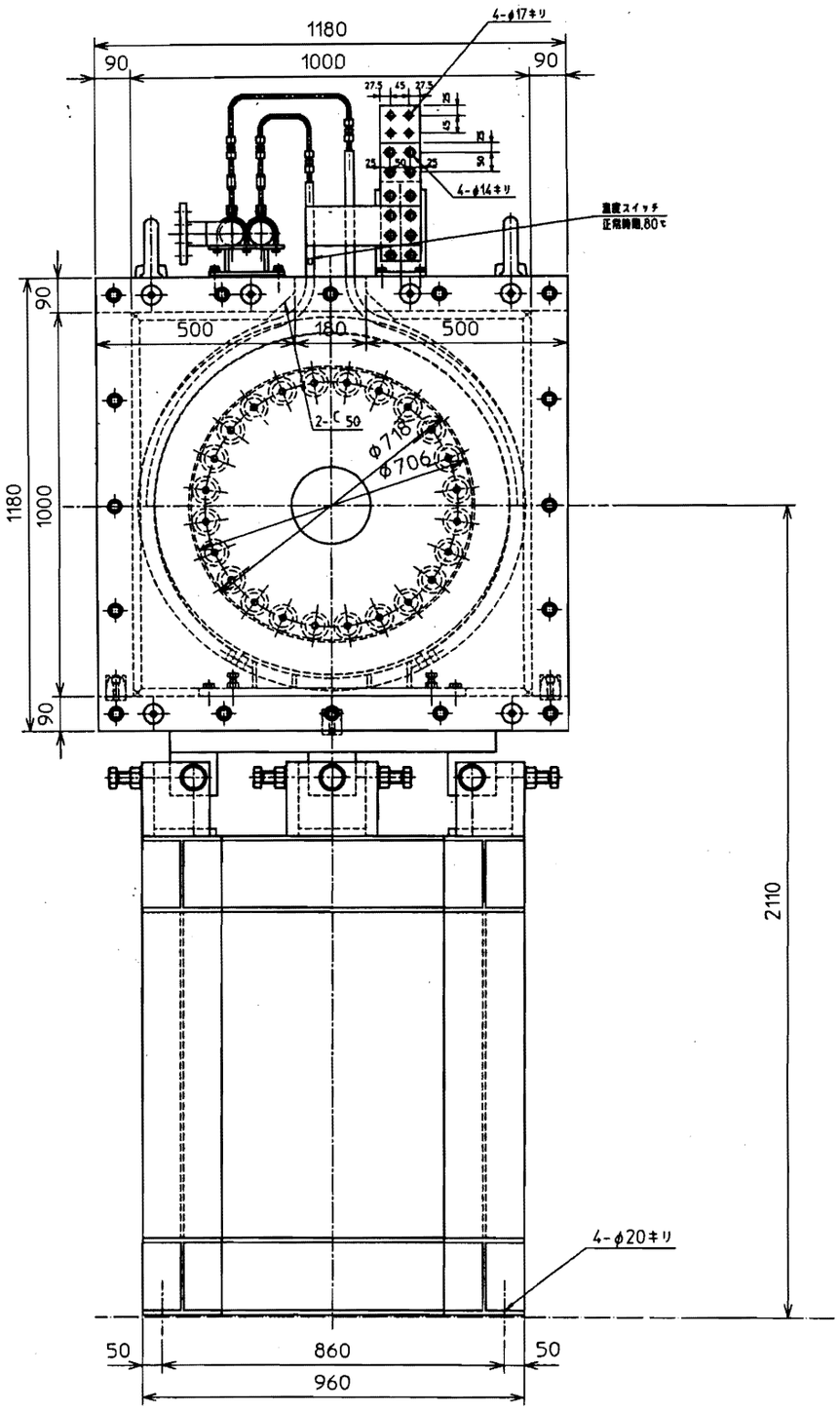

Figure 2.10: A drawing of solenoid magnet

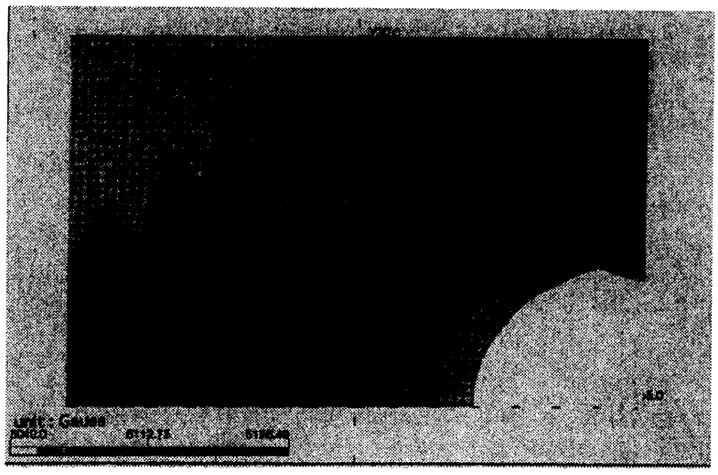

Figure 2.11: A typical result of the calculation of the magnetic field for XZ plane with TOSCA

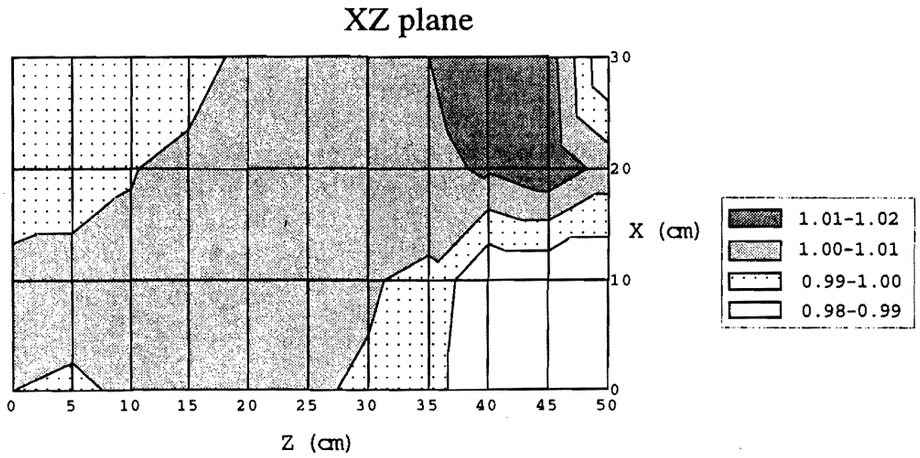

Figure 2.12: A contour plot of the measured magnetic field inside the solenoid magnet; XZ plane

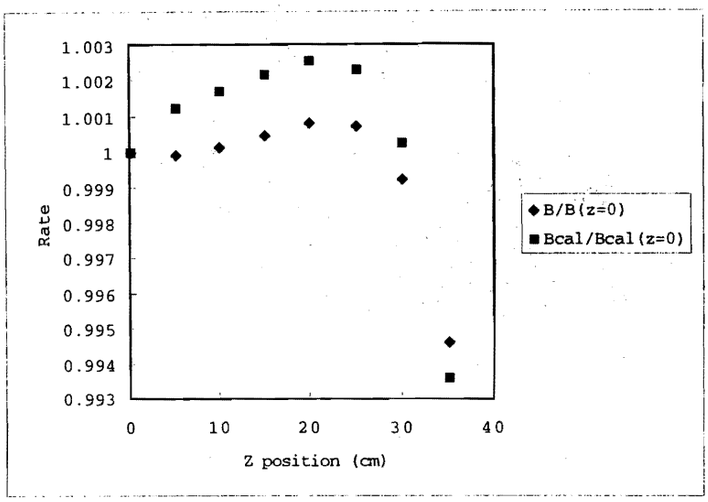

Figure 2.13: A plot of variation rate along the line (0,0,z); z 0∼ 45 cm by 5 cm step, normalized at the value of the center of the magnet; (0,0,0)

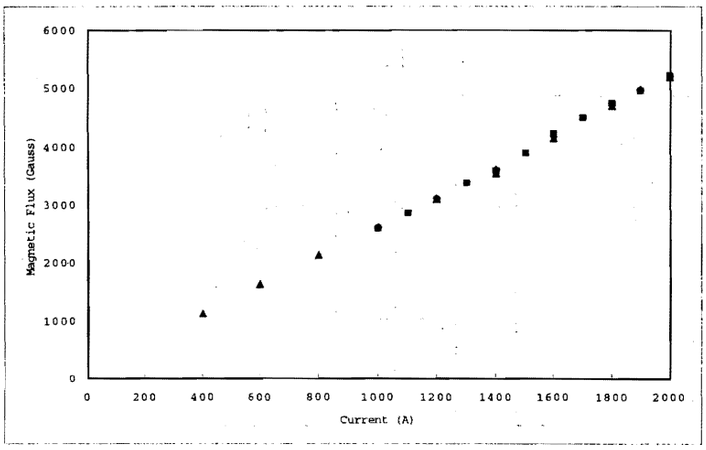

Figure 2.14: Magnet flux vs. applied current

Chapter 3

Experiment

3.1 Overview

Experiment E906 was carried out at D-6 line of the Alternated Gradient Acceralator (AGS) at Brookhaven National Laboratory. The D-6 line experimental hall was built in 1990 for experiment E813 (H dibaryon search).

Fig 3.1, shows a schematic layout of the experimental setup which includes 1) a magnetic spectrometer to identify the reaction $K^-p \rightarrow K^+\Xi^-$, and 2) a Cylindrical Detector System to measure the sequential decaying $\pi^-$from S=-2 system.

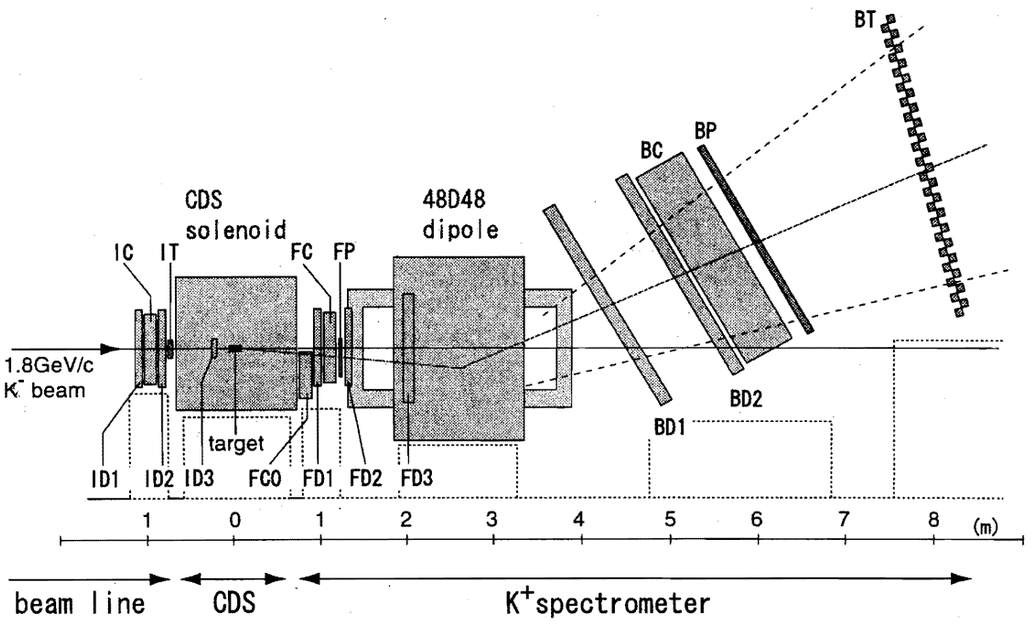

Figure 3.1: A schematic drawing of D-6 line experimental hall of AGS

In Fig 3.2, a schematic view of 2 GeV/c K^- beam line is shown. The beam

line delivered 1.8 GeV/c K^-mesons to create Ξ^-hyperons with $K^-p \rightarrow K^+\Xi^-$ reactions in the targets of Be and CH2. In the beam line, three scintillator hodoscopes (MP,MT and IT), an aerogel Ĉerenkov counter (IC) and three drift chambers (ID1-3) were installed for identification and tracking of the K^- beam. The outgoing K^+ was analyzed with a magnetic spectrometer placed downstream of the target. The magnetic field was 1.4 Tesla at the center of a dipole magnet (48D48). The field direction was horizontal and thus outgoing particles were bent up vertically. The K^+ was identified by the measured momentum and velocity calculated from the time-of-flight (TOF) data and the path length. The momentum was derived from the trajectory which was reconstructed with five drift chambers (FD1-3 and BD1-2). The TOF information was obtained from data on a time-of-flight array (BT) which was installed at the end of the spectrometer. Background particles in the K^+ identification were mainly pions and protons. Two aerogel Ĉerenkov counters (FC and BC) differentiated the K^+ from the π^+. A lucite Ĉerenkov counter (FC0) eliminated the knock-out protons by incident K^-'s. Two scintillator hodoscopes (FP and BP) were used to form a primary on-line trigger.

We installed CDS in the target section to detect the decaying particle from (K^-, K^+) reaction in the target.

Most beam line and spectrometer elements had been fabricated for experiment E813, and some were rebuilt or modified to be suitable for our experiment.

3.1.1 2 GeV/c K^- beam line

We obtained a high intensity 1.8 GeV/c K^- beam at D-6 line experimental hall of BNL-AGS. Details of this beam line are given in [25].

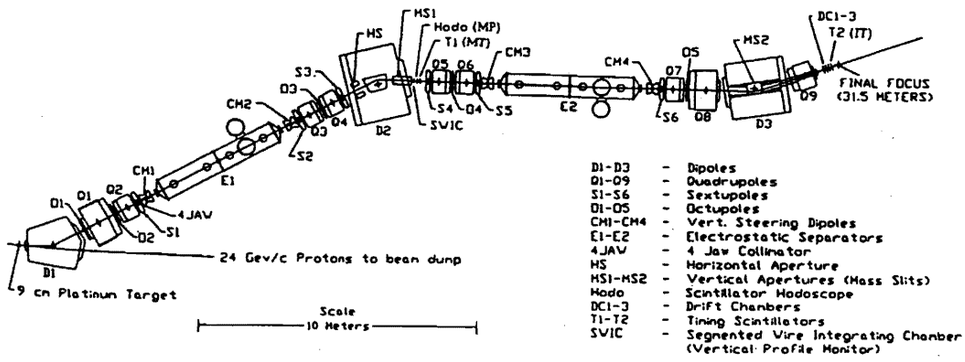

Figure 3.2: A schematic view of the BNL-AGS 2GeV/c K^- beam line

A schematic view of 1.8 GeV/c K^- beam line is shown in Fig 3.2. The beam line elements include three dipoles (D1-3), nine quadrupoles (Q1-9), six sextupoles (S1-6), five octupoles (O1-5), two velocity selectors with separated E and B fields (E1,2 and CM1-4), and collimaters (4-Jaw, HS and MS1,2).

Primary protons accelerated to 24 GeV/c by the AGS are incident on a 9 cm-thick platinum target located at the entrance of the first dipole (D1). Secondary particles are transported with extraction angle of 5 deg and a momentum acceptance of ±3% (FWHM). After the velocity is selected with two stages of separators (CM1-E1-CM2 and CM3-E2-CM4), they are delivered to the final focus point (FF). In Table 3.1 are summarized the design parameters of the beam line.

Table 3.1: Design parameters of the AGS 2 GeV/c kaon beam line

Beam line length		31.4 m
Momentum range		up to 2 GeV/c
Production target	material	platinum
	length×width× height	9.0×0.7×1.0 cm^3
Central production angle		5 deg
Momentum acceptance		±3% (FWHM)
Separators; E1 and E2	voltage	750 kV
	size	4.5 m long, 10 cm gap
Solid angle		6.2-6.5 msr
momentum acceptance		(MS1=3 mm,MS2=4 mm)

During the run of fiscal year 1998, K^- flux was, typically, more than 2.0×10^6 /spill and π/K ratio was about 2, when 10×10^{12} primary beam hit the production target, and the two separators were running at 700 kV each with the mass-slit openings of 0.14" for MS1 and 0.19" for MS2.

3.1.2 Spectrometer Instrumentation

Spectrometer Magnet(48D48)

A BNL 48D48 dipole magnet(48"pole length by 48"width) with a gap of 80 cm was used for the spectrometer. A booster coil was added to reach the desired field with minimum field degradation due to the wide gap. The central magnetic field was set to 1.4 Tesla in the experiment. The field direction was horizontal and thus outgoing particles were bent vertically.

Scintillator Hodoscope

In Table 3.2 are summarized the specifications of five scintillator hodoscopes, MP, MT, IT, FP and BP. The hodoscopes MP and MT were installed downstream of the first mass slit MS1 (see Fig 3.2). The primary function of MP was the determination of the beam momentum by measuring the X position of the particle, whereas that of MT is the measurement of the time-of-flight of the beam to IT. The hodoscope IT with the intrinsic resolution of 60 psec in sigma provided the reference timing signal, as the start counter, for all the detectors. For our experiment, a downsized IT was

fabricated. For particles produced at the target center, the out-of-beam elements (#1-#11) of FP gave a vertical angular coverage of $-13.2 \leq \theta_Y \leq -1.5$ deg, and the top four elements (#12-#16) of FP were not used due to the incident beam hitting the modules directly, whereas BP gave a horizontal coverage of $|\theta_X| \leq 6.4$ deg.

Table 3.2: Specifications of the scintillator hodoscopes. The orientation is indicated by the direction of hodoscope slats (V:vertical, H:horizontal).

	Orientation	Segmentation	Dimension of each element length × width × thickness (cm^3)
MT	V	72	1.5 × 3.7 × 0.6
MP	V	9	1.5 × 0.7 × 0.3
IT	H	1	10.0 × 4.0 × 1.0
FP	H	16	24.0 × 1.5 × 0.4
BP	V	6	180.0 × 21.0 × 1.0

Drift Chambers

The spectrometer was instrumented with three drift chambers (ID1-3) to measure the track of an incident beam particle and five drift chambers (FD1-3 and BD1-2) to reconstruct the track of an outgoing particle through the magnet. Table3.3 shows the specification of these drift chambers. In the outgoing channel, a particle was bent vertically in the spectrometer, and the vertical position of the hit was related to its momentum. Therefore, FD1-3 and BD1-2 were designed with a plane configuration of y-u-v to have a better resolution in Y measurements. In contrast, ID1-2 were designed with a plane configuration of x-u-v to give a better resolution in X measurements which were related to the beam momentum. ID3 was especially fabricated for E906 experiment because we don't have enough space to put another chamber in the upstream of the Solenoid magnet. In order to get a better vertex resolution of (K^-, K^+) reaction, it was installed in just front of the target inside the CDS. ID3 were designed to have 4 planes with a configuration of u-u',v-v'. The gas mixture used to operate all of these drift chambers was 77% argon, 20% isobutain and 3 % methylal, which had been shown to have good chamber aging characteristics.

The two beam drift chambers ID1-2 were identical and so were FD1 and FD2. The drift cell of these chambers were designed for operation at a high beam rate. Sense wires were positioned with a 5.1 mm (0.2") spacing and thus the maximum drift distance was 2.5 mm, giving the maximum drift time of 50 nsec. ID3 is a small chamber, whose sense wire spacing is 4.23 mm and maximum drift distance was 2.1 mm, giving the maximum drift time of 40 nsec. The chamber FD3 was installed inside the magnet for better determination of the momentum. It provided fast outputs of Y hits for a second-level trigger, which is described later. The chambers

BD1 and BD2 had the active area of 124 cm×224. They had a similar design of drift cells with sense wires placed with 2.0 cm spacing. The position resolution in sigma of these drift chambers were 0.2 mm for ID1-2 and FD1-2, 0.3 mm for FD3 and 0.4 mm for BD1-2.

Ĉerenkov Counters

We installed four Ĉerenkov Counters to separate the kaons in Ξ^- production from the background, pion and proton.

In order to separate K^- from π^- in the 1.8 GeV/c beam, the aerogel Ĉerenkov counter IC with a refractive index of 1.03 was used. Before the fiscal 1997 run, we fabricated the down-sized new IC. Fig3.3 shows a schematic drawings of IC.

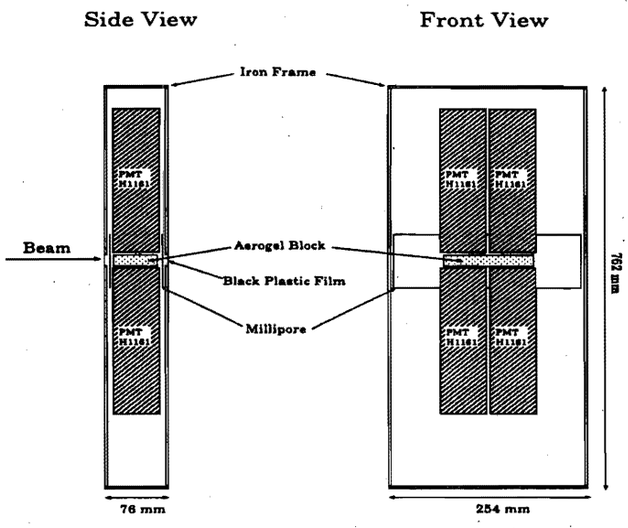

Figure 3.3: A schematic drawing of the new IC

For the separation of outgoing K^-'s from π^-'s, two aerogel Ĉerenkov counters FC and BC, both with index of refraction n of 1.04, were install in the spectrometer. FC is located between FP and FD1. The function of BC, located downstream of the magnet, was the rejection of background pions, muons and electrons originating from in-flight decay of incident K^-'s and also from secondary interactions of non-interacting beams.

FC0 was installed in front of FC to eliminate the knock-out proton , that appeared to be a $K^+$from the (K^-, K^+) reaction. Fig 3.4 shows a schematic drawings of FC0.

In Table 3.4 are summarized the specifications of each counter. We had good quality dry aerogel for IC and FC. As for IC, the radiator cell was viewed by four

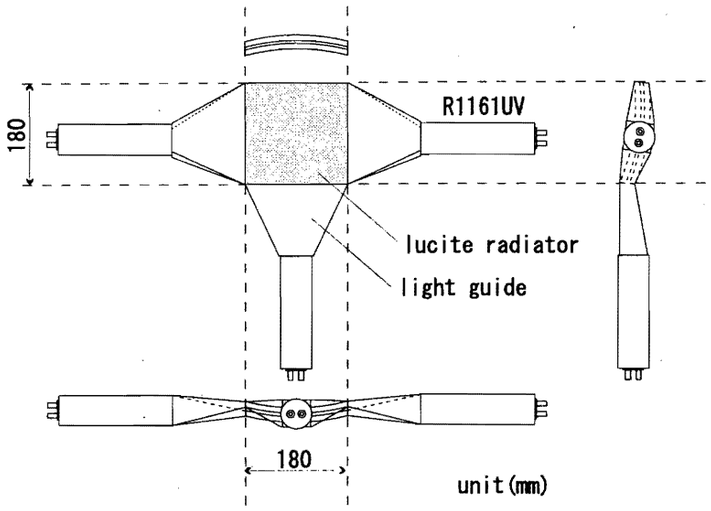

Figure 3.4: A schematic drawing of the FC0

PMT and the four readout signals summed up to detect the Ĉerenkov photon. We use the 2" PMT's (Hamamatsu H1161) for IC in order to reduce the thickness of elements in beam direction. As for FC, the four 3" Finemesh PMT's (Hamamatsu H6155-01) were used and the four readout were summed up as well as IC. They were installed in the iron box to prevent loss of transparency due to water absorption. They were operated in beam at high counting rates, equipped with PMT's with booster power supplies to hold potentials. Booster power was supplied to the last three dynodes for IC, and the last four dynodes for FC.

For FC and BC, the high voltages supplied to each PMT were adjusted to give an equal gain for a detected photon and the position of the single photo-electron peak in ADC spectrum was monitored by flashing green LED's installed in the devices.

The aerogel blocks used for BC were manufactured by the Air-glass Company in Sweden. Aerogel blocks were kept in dry nitrogen gas to prevent from change in transparency, but device performance had been worse due to deterioration from hydration until 1997's run. We dried all of the radiators of BC before starting 1998's run. Each PMT of BC was placed inside a 1/4"-thick magnetic shield of iron. The use of a μ-metal pipe extended by about 3" from the cathode surface was effective in reducing the magnetic field effect on the performance of the PMT. A collar of aluminized mylar was installed in front of the PMT to increase the light yield[26]. Output pulses from 40 PMT's were linearly added to obtained ADC spectrum.

The aerogel radiator cells of these devices were coated with highly reflective white paper(Milipore) to prevent loss of Ĉerenkov light.

FC0 was a differential Ĉerenkov counter using a lucite block. Fig 3.4 shows a schematic view of FC0. The block was shaped from a part of the sphere whose diameter was 70 cm. The thickness was 1 cm. Three PMT's were mounted on FC0

through light guides. The device was also installed in an iron box. It was designed and built for experiment E906.

The devices were tested with the 48D48 magnet on. Based on studying the threshold of the IC's ADC spectrum, 15% π^- contamination for 1.8 GeV/c incident was allowed in order not to lose kaons beam. Studying the counts below the applied threshold of ADC spectrum, inefficiencies for 1.4 GeV/c pions were less than 2.5% for FC and 2.0% for BC. Identifying the scattered particle by studying the correlation between IT-BT time of flight information and the momentum analyzed by 48D48 spectrometer, inefficiency for 1.4GeV/c proton is 70% for FC0, where K^- efficiency is about 92 %.

Time-of-flight Array(BT)

The time-of-flight array BT was located at the end of the spectrometer to measure TOF's of outgoing particles. The typical flight length was 7.9 m from the target, giving TOF difference of 1.8 nsec between the K^+ and π^+ at a momentum of 1.25 GeV/c. Details of the design and the device performance were described in Ref[27]. The array consisted of 40 logs of plastic scintillators(BICRON BC-408). Each scintillator log was 200.0 cm long, 8.5 cm wide and 5.0 cm thick. Each end was directly coupled to 2"-diameter PMT(Hamamatsu H1949) without a light guide. The signal from each anode was discriminated and the timing signals were then read by Kinetics F432 FASTBUS TDC and also by LeCroy FERA/FERET system to provide a fast conversion of signals for the second-level trigger.

The whole array was tested with the beam by changing the field of the magnet, and the TOF resolution averaged over 40 elements was found to be 130 psec in sigma. By unfolding the resolution of the START signal (60 psec), the intrinsic timing resolution of 110 psec in sigma was obtained.

3.1.3 Trigger

The event triggers were formed by using signals from the hodoscopes (IT, FP, BP, CDH), the Čerenkov counters (IC, FC, FC0, BC). In Table 3.5 are summarized the definitions of event triggers used for the data taking in the 1998 run, typical event rates per spill and adopted prescale factors.

Triggers for (K^-, K^+) reactions were KK and KKCDH. The main trigger was the KKCDH trigger which means that at least one decaying particle was detected by the CDS following (K^-, K^+) reaction in the target.

In the run, events with different types of triggers were taken simultaneously with appropriate pre-scale factors which are shown in Table 3.5. For each event, a bit was set with a CAMAC input register for distinguishing the trigger types of reactions in the off-line analysis. The rate for the KK trigger was typically 350 per 1.0×10^6 K^- 's incident on the target, while it was reduced to 140 for the KKCDH trigger. As I mentioned in the Čerenkov section, KSCAT included a lot of protons knocked out by incident K^-. Further reduction of the trigger rate was achieved by rejecting

proton events with the second-level trigger based on a front-end computer. The rejection was done based on TOF difference between protons and kaons. The bottom half of the FD3 y-y' planes were segmented to give 16-bit information of vertical hit positions by which the momenta of outgoing particles were roughly determined combined with BT. Signals from BT were digitized by the LeCroy FERA/FERET system to provide fast TOF information of hits. With this second-level trigger, the event rate was reduced to 30, and the live time of data acquisition system was more than 80% of the total running time.

3.1.4 Data Acquisition and Monitoring

The data acquisition system had been developed based on the one used in the CERN NA36 experiment[28]. The kernel of the system was a pair of VME-based microprocessors (FIC 1&2), one for the event readout and the other for the event building and output to an Exabyte 8mm tape drive. The latter served also for on-line monitoring. The device signals were processed mostly with FASTBUS ADC's and TDC's. Discriminated signals from the drift chambers of the beam line and the spectrometer, about 2400 channels in total, were digitized by LeCroy 1879 pipeline TDC's. We use LeCroy 1877 multi-hit TDC's for CDC's discriminated signals. Outputs from PMT's, about 150 channels in total, were divided into two; one fed to a LeCroy 1885F ADC for pulse height measurements and the other fed to a Kinetics F432 high resolution TDC (25psec/ch) for timing measurements. A signal from CDZ was measured with LeCroy 1885F ADC's for pulse height. The DAQ system included also several CAMAC modules to process scaler data and the trigger bits. Scaler information was read out either event-by-event or spill-by-spill, depending on the purpose.

For on-line monitoring, a sample of data was transferred to a VAX computer through a dual-ported Q-bus/VME memory from BIT3. The data were also transferred from the host computer to other workstations linked through Ethernet. The on-line monitoring was made with a package called "IDA (Interactive Data Analyzer)" The IDA had various processes running at a time. One of such processed was called "OPERATOR" to control the event analysis (start and stop the analysis, for example). A program called "HVIEW" displayed histograms defined by users. There were also programs such as "EVIEW" to display a view of each event and "NORMON" for monitoring of scaler information.

Table 3.3: Design parameters of drift chambers used in the experiment.

	Plane	Orient-ation	Sense wire Spacing(mm)	#channel	Active area X×Y(cm^2)	Location Z(cm)	Sigma (mm)
	u-u'	120deg	5.08	24×2			
ID1	v-v'	60deg	5.08	24×2	12.2×10.6	-92.3(cm)	0.2
	x-x'	0deg	5.08	24×2			
	u-u'	120deg	5.08	24×2			
ID2	v-v'	60deg	5.08	24×2	12.2×10.6	-77.7(cm)	0.2
	x-x'	0deg	5.08	24×2			
ID3	u-u'	-45deg	4.23	10×2	5.5×1.5	-20(cm)	0.2
	v-v'	45deg	4.23	10×2			
	u-u'	210deg	5.08	48×2			
FD1	v-v'	150deg	5.08	48×2	21.2×24.4	78.7(cm)	0.2
	y-y'	90deg	5.08	48×2			
	u-u'	210deg	5.08	48×2			
FD2	v-v'	150deg	5.08	48×2	12.2×10.6	112.4(cm)	0.2
	y-y'	90deg	5.08	48×2			
	u	150deg	12.7	64			
FD3	y	90deg	12.7	64	45.7×81.3	191.4(cm)	0.3
	y'	90deg	12.7	64			
	v	30deg	12.7	64			
	y	90deg	20.0	112			
BD1	u	120deg	20.0	128	114.0×214.0	415.5(cm)	0.4
	v	60deg	20.0	128			
	y'	90deg	20.0	112			
	y	90deg	20.0	112			
	u	120deg	20.0	128			
BD2	v	60deg	20.0	128	114.0×214.0	498.3(cm)	0.4
	y'	90deg	20.0	112			
	v'	60deg	20.0	128			

The sense wires of x' plane are located at the position shifted from the sense wires of x plane by the half size of the cell. The notation for other planes is same as this.

Table 3.4: Design parameters of aerogel Ĉerenkov counters

	IC	FC	FC0	BC
Effective area (X×Ycm^2)	11.5×2.0	25.0×25.0	18.0×18.0	126×189
Total thickness(cm)	5.8	9.0	1.0	9.0
Refractive index	1.03	1.04	1.5	1.04
Threshold momentum for π/K (GeV/c)	0.56/1.97	0.49/1.74	-	0.49/1.74
PMT	Hamamatsu R1161UV	Hamamatsu H6155-01UV	Hamamatsu R1161UV	Burle 8854
Number of channel	4	4	3	40

Table 3.5: Definition of the on-line triggers. The typical rate per spill and prescale factor used for the data taking are also shown

Bit	Definition	Rate/spill	Prescale factor
KBEAM	IT∩$\overline{\text{IC}}$	1.0×10^6	4×10^4
PIBEAM	IT∩IC	2.0×10^6	1×10^6
KSCAT	FP∩BP∩$\overline{(\text{FC} \cup \text{BC})}$	-	-
PISCAT	FP∩BP∩(FC∪BC)	-	-
PIPI	PIBEAM∪PISCAT	3800	-
PIK	PIBEAM∪KSCAT	350	-
KPI	KBEAM∪PISCAT	1500	200
KK	KBEAM∪KSCAT	350	20
KKCDH hold	KK∩CDH	140	-
KKCDH passed 2nd-level	KK∩CDH	30	1

Chapter 4

Analysis

In this chapter, the procedures for the data analysis are described. The experiment for the $\Lambda\Lambda$ hypernucleus is decomposed into two measurements; identification of Ξ^- produced via (K^-, K^+) reaction and measurement of the sequential decaying π^- from the $\Lambda\Lambda$ hypernuclei. The performance of each measurement is evaluated based on the data collected in 1998.

At first, the calibration procedures and the evaluation of the performance of the CDS are explained in Section 1. Section 2 shows the identification of Ξ^- production by 48D48 spectrometer system. In the last section, the identification of $\Lambda\Lambda$ hypernucleus is described.

4.1 Calibration of the CDS

In this section, calibration of the CDS is explained. As I mentioned in Chapter 2, it was unfortunate that Z-chamber could not be operated due to break-down of many wires. The CDC calibration process is mainly described here. We took several sets of the calibration data. The cosmic ray data is used to determine the XT functions of CDS. We study the various performances of the CDS with the data of π^- elastic scattering with a slat target made of polyethylene. The momentum scale was calibrated by the momentum of π^+ from Σ^+ stopped in the target.

4.1.1 Helical-track Reconstructing Module (HRM)

An analysis program; Helical-track Reconstructing Module (HRM), for the CDS was developed mainly by T. Tamagawa, who is a member of E906. This software roughly consists of three parts; the track finding, the fitting and the vertex reconstruction.

The track finding part gives the data set which constitutes a track by matching the possible hit pattern, and prepares the several candidates of the initial track parameter for each track. The fitting part starts fitting with these initial parameters and derives the fitted track parameters by the least square method. The vertex reconstruction part categorizes the event according to the topology. For example, an event contains two negative and one positive tracks is categorized into the candidate

of Ξ^-. The category of $\Lambda\Lambda$ hypernuclei consists of those events which have only two negative tracks.

An event display was implemented using HIGZ package of CERNLIB. We can easily survey the whole system; an example of the event display is shown in Fig 4.1. This shows a typical event of Ξ^- decay.

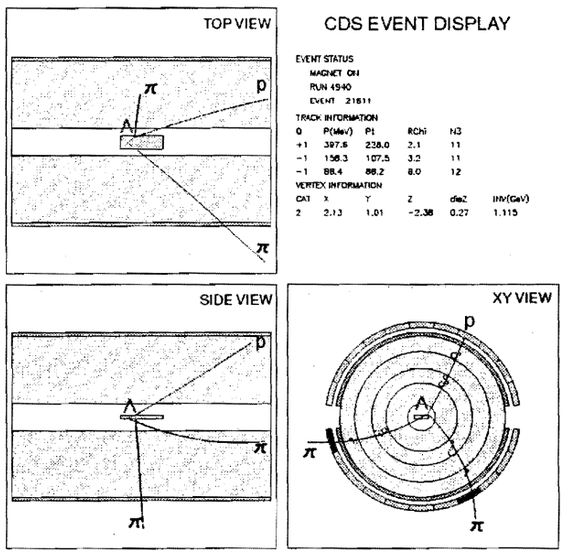

Figure 4.1: An example of the event display

4.1.2 XT function process with cosmic ray data

Just before starting the physics run, we took several sets of the cosmic ray data with the solenoid magnet turned on. We used this to determine the XT function of the CDC, which is the relation function between the drift time (T) of the electron and the drift length (X). The function is calibrated for each layer. A cosmic ray was triggered by two CDH segments facing each other across the CDC. We accepted only those rays which traversed the CDC from one side to the other completely and left more than 22 layers hit for the calibration.

XT functions were processed by repetition of the following procedure. At first, drift circles of hit cells are assumed by a trial XT functions. Secondly, a track is reconstructed by fitting a set of drift circles except for a remarked layer's drift circles, and the closest distance "X" between the reconstructed track and the sense wire of the remarked cell are calculated. In the third, the pair of X and time information from TDC are accumulated for each layer. A number of XT pairs is plotted in two dimmensioanl histogram, and the scattered image is fitted by a function to make a next trial XT function. The fitting function is : $X(T) = A0 + A1 \times T + A2 \times T^2 + A3 \times T^3 + A4 \times sqrt(T)$

This procedure was iterated until the average of residual of all layers was unchanged. In Fig 4.2, a typical scatter XT plot is shown.

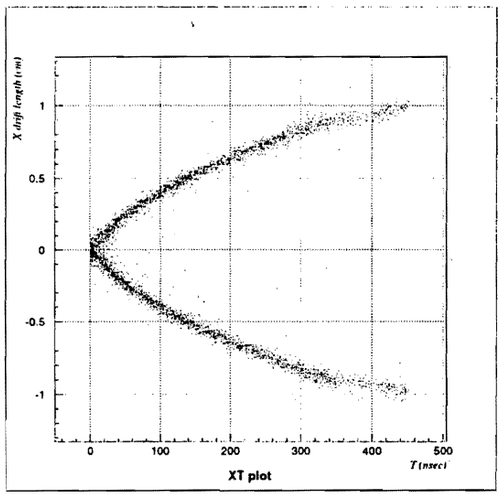

Figure 4.2: A typical XT plot; layer 4

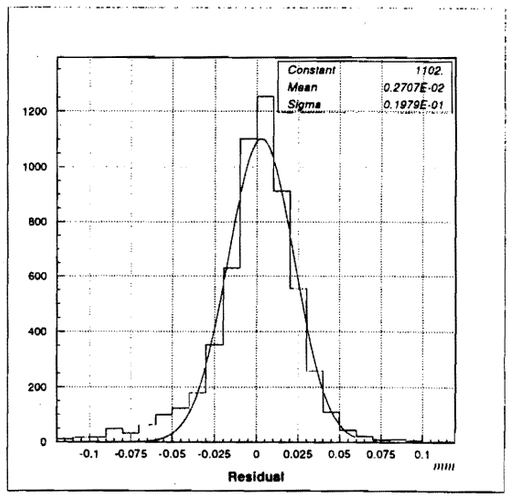

Figure 4.3: The residual of layer 4

The final XT function gives the residuals of each layer, Fig 4.3 shows a histogram of the residual of layer 4.

The results of the residuals is summarized in table 4.1. The residuals in the table 4.1 include the contributions from multiple scattering and the tracking error at the respective layer. When we assume the momentum of cosmic ray to be 1 GeV/c, the effect from multiple scattering is equivalent to 60 μm in the spatial resolution. The approximate formula of the tracking error is given in [29], which is a function of the layer's geometry. This formula gives the tracking error at an arbitrary point along the track, and the error is calculated to be 35% of the intrinsic resolution on average. When we account for these effects, the intrinsic resolution is estimated to be 230 μm.

At last, I should mention that, since we could not supply enough voltage on layer 12, the efficiency of layer 12 was unfortunately so small that layer 12 did not participate in the tracking.

Vertex resolution

The vertex resolution was studied with π^-scattering on a slat target. The target was made of polyethylene and is shown schematically in Fig 4.4.

Incident π^-, whose momentum is 1.4 GeV/c, scatters elastically with a proton in the target. CDS then detects two tracks of proton and π^-. The vertex point is reconstructed by assuming the center of two points which give the closest distance between two tracks projected on the X-Y plane. A histogram of the reconstructed target image in z direction is shown in Fig 4.5.

Table 4.1: A result of the residuals of all layers

# Layer	Residual(μm)
1	272
2	263
3	254
4	198
5	203
6	185
7	281
8	328
9	375
10	209
11	209
12	-
Ave.	252

The cut conditions are that the reduced chi-square of the fitting is less than 5 and the vertex information in x and y direction is inside the target region. This shows the slat target image very clearly, which gives the vertex resolution of z direction is 3.7 mm in sigma. This corresponds to 200~240 μm of the CDC's intrinsic resolution in r-ϕ plane.

The vertex resolution in x-y plane was given by the image of the frame of the silicon strip detector(SSD). We tried to introduce the SSD's to get the vertex resolution better, but in vain. The environment in experimental hall, temperature and humidity, is very hard for the SSD's to be operated properly.

SSD's still were installed during taking the data with the slat target and the π^-beam was broad enough to scatter in the frame of SSD's, whose thickness is 2 mm. Fig 4.6 shows a histogram of the vertex in y axis which originates from the SSD's frame. The image gives a sigma of 1.2 mm, which corresponds to a vertex resolution of 1 mm in the y axis.

The geometry of CDS is symmetry in the r-ϕ plane, which means that the resolution in the x direction is the same as in the y direction. A Monte Carlo simulation was done: it gives us the same vertex resolution in x as in y.

4.1.3 Momentum calibration of CDS

The momentum scale of CDS is calibrated by observing the π^+ from the decay of stopped/in-flight Σ^+ produced in the (K^-, π^-) reaction with a CH_2 target. A Σ^+ was produced via a (K^-, π^-) reaction with the incident K^- whose momentum was 1.4 GeV/c. The momentum of outgoing π^-'s was analyzed by the 48D48 spectrometer system. The particle originating from in-flight K^+ decay also goes into

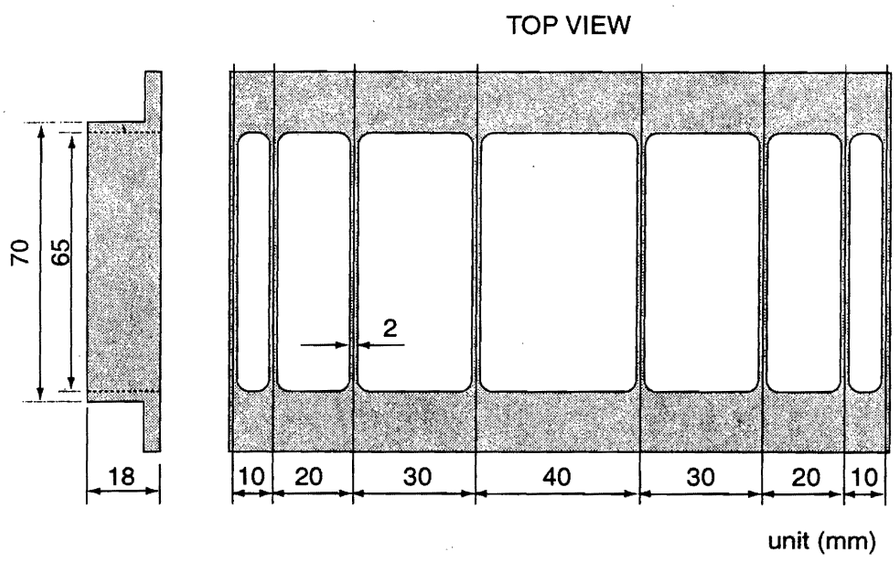

Figure 4.4: A schematic drawing of the slat target

the spectrometer, and contaminates the π^+ spectrum. Fig 4.7 shows spectra of the reconstructed missing mass, assuming the $K^-p \rightarrow \pi^-X$ reaction. The left-hand side spectrum consists of the all data, which shows a peak on top of the broad background. The right-hand side is the spectrum where the outgoing momentum is gated from 1.12 to 1.24, where we select the Σ^+ around 1.19 GeV/c^2.

The stop position of Σ^+ in the target is estimated using a calculation of the stopping range. The Σ^+ decay event leaves only one positive track in CDS, which is not enough to reconstruct the depth of recoiled Σ^+stopping in the target. Therefore, the range of Σ^+ was calculated with the missing momentum using the Zieglar formalism, which gives more precise energy loss information for low energy particle.

Fig 4.8 shows a momentum spectrum of π^+ from Σ^+ decay, where the peak of the missing mass less than 1.19 GeV/c^2 is gated. Events in the lower half of missing mass is expected to stop in the target more easily.

It consists of a peak of the stopped-Σ^+ and a broad bump from in-flight decay. The component of in-flight decay shows a slightly asymmetric shape with a tail to higher momentum, which is caused by the CDS acceptance. When the histogram from 0.14 to 0.22 GeV/c was fitted with two gaussians, it gives a centroid of stopped Σ^+peak; 184.7 ± 1.9 MeV/c and the width; 7.07 ± 1.91 MeV/c, whereas the momentum of π^+ from Σ^+ decay is known to be 184.6 MeV/c.

In searching for $\Lambda\Lambda$ hypernuclei among $2\pi^-$ data, a large enhancement is observed, which corresponds to the decay from the twin hypernuclear production, ${}^{4}_{\Lambda}$H and ${}^{3}_{\Lambda}$H; This gives two more calibration points for the π^- momentum. The details will be described in the Chapter 5.

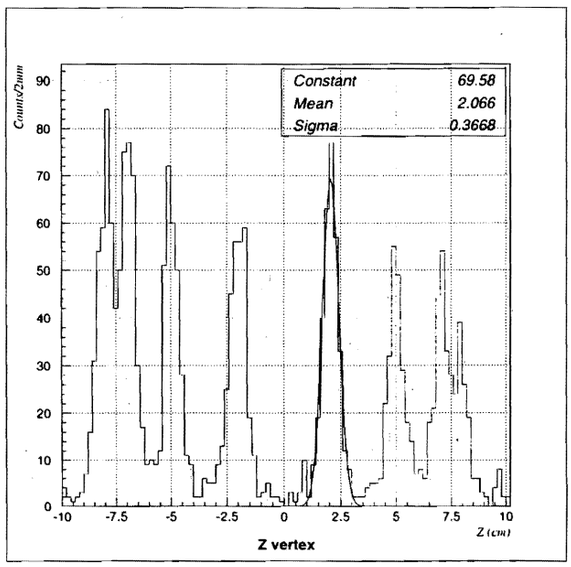

Figure 4.5: A histogram of the slat target image in z direction

4.1.4 Total momentum resolution of the experiment

For this experimental principle, we cannot ignore the contribution of energy loss correction to the momentum resolution. The energy loss in the material has some straggling by statistical nature and the vertex resolution also affects the amount of energy loss correction. An estimate of these effects as a function of the particle momentum is shown in the top of Fig 4.9. A distribution of energy straggling is evaluated by an average flight length in the target of 1 cm. The vertex resolution of 1 mm in sigma was taken into account to estimate the error of energy loss correction.

Adding these two effects to the resolution, which has been shown in Chapter 2, in quadrature gives the total momentum resolution. The bottom of Fig 4.9 presents a result where the dip angle is 60 degrees. The Σ^+ decay data was also plotted in this figure; the data point of the Σ^+ calibration agrees with the curve within a sigma.

According to this estimation, the momentum resolution at 100 MeV/c π^- is expected to be 3.6 MeV/c in sigma.

4.1.5 Efficiency of the track reconstruction by CDC

The CDS track reconstruction efficiency was studied using the π^--p elastic scattering data set.

At first, the hitting efficiency of each layer was studied. Table 4.2 shows the hitting efficiency of each layer; Eff_{hit}, where $Eff_{hit} = \frac{N_{find}}{N_{good}}$. N_{good} means the number of good events where all layers have the hit information except for a specific

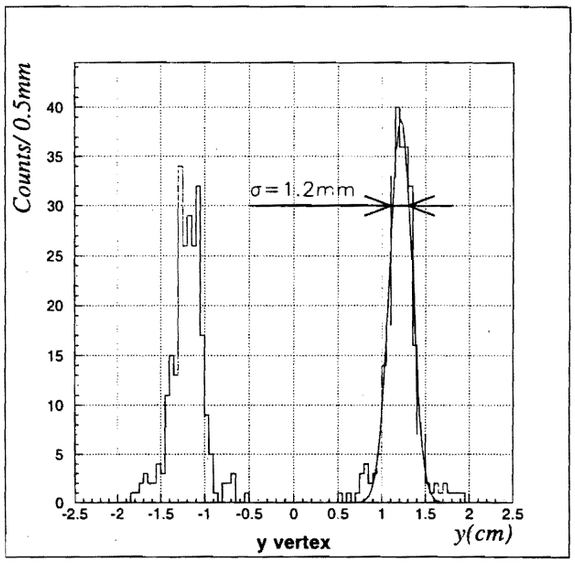

Figure 4.6: A histogram of the vertex in y direction which is caused by the SSD's frame

layer, and N_{find} means the number of events where a corresponding hit is found at the respected layer. This gives the possibility of the event in which all layers have hit information to be 0.744.

Table 4.2: Hitting efficiency of each layer

layer	Eff_{hit}	layer	Eff_{hit}
1	0.953	7	0.993
2	0.995	8	0.996
3	0.999	9	0.992
4	0.951	10	0.993
5	0.928	11	0.926
6	0.987	all	0.744

Secondly, we studied the tracking efficiency of HRM, Eff_{track} using a data set of the excellent events, which only consist of two "back to back" excellent tracks with 11 layers hits, and the total off-line analysis efficiency, Eff is given.

When HRM is going to find a track, we required a tracking criterion in order to keep the tracking quality better. The criteria are the number of the hit layer is at least 9 and layer 1,2,5,8,10 and 11 always have hit information. Table 4.3 shows all of allowed hit configurations that can satisfy the requirement, and the probability of taking these configuration; P_{hit} is derived by the Table 4.2. Eff_{track} is the tracking

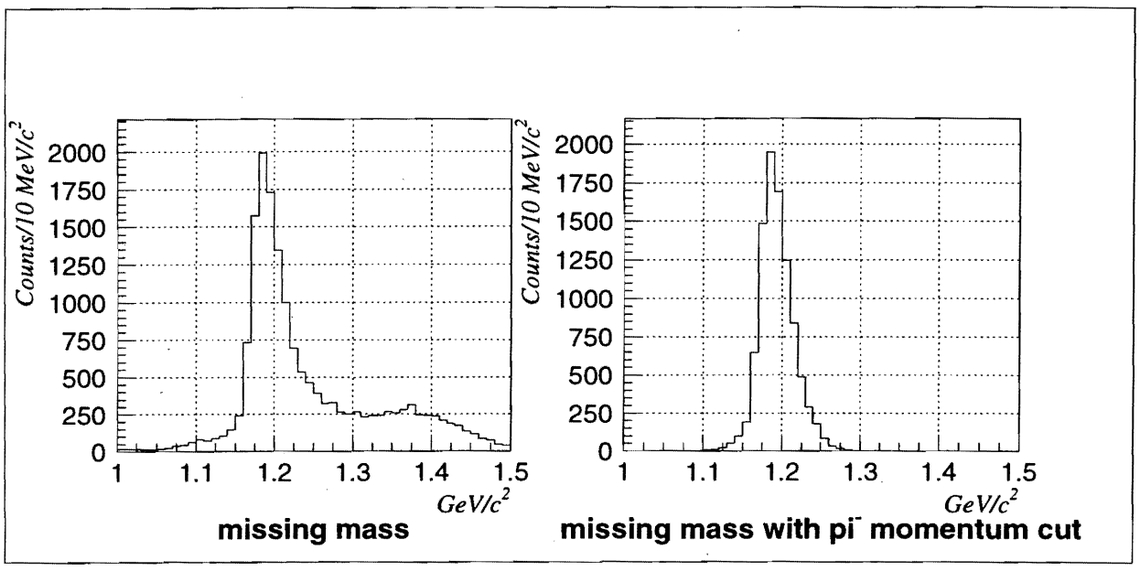

Figure 4.7: histogram of the missing mass of (K^-, π^-)reaction

efficiency of passing the following conditions; HRM can recognize the existence of track, reduced chi-square of fitting is less than 5, the reconstructed track points to the hit CDH and the sign of particle agrees with the PID by the TOF information.

In tabel 4.3, the Eff_{track} of excellent events is shown to be 0.810 is shown, which is derived with analyzing the mock data of the excellent track generated by a simulation code. The simulation code generates the mock data which consists of the set of layer#, cell# and drift length. HRM can read the mock data and analyze it as well as the real data. HRM cannot necessarily succeed in reconstructing the track, even though the excellent event requires all layers to be hit. The Eff_{track}'s missing one or two layer is derived by tracking with masking the correspond layer information of the real excellent data.

This study gives us the total off-line analysis efficiency per track to be 64.7 %.

4.1.6 Timing resolution of CDH

The timing resolution of the CDH's is also studied with the slat target data. The time-of-flight information between the reaction vertex and CDH was given by subtracting the TOF from IT to the vertex from the TOF from IT to CDH.

Fig 4.10 shows a scatter plot of the measured momentum vs. the reconstructed beta with the TOF information, where the kinematics line is also shown.

Fig 4.11 shows a histogram of residual of CDH timing information. The residual is given by subtracting TOF information from the reconstructed time with the path length and the particle momentum. The histogram also shows the fitted results and gives the width as 250 psec in sigma.

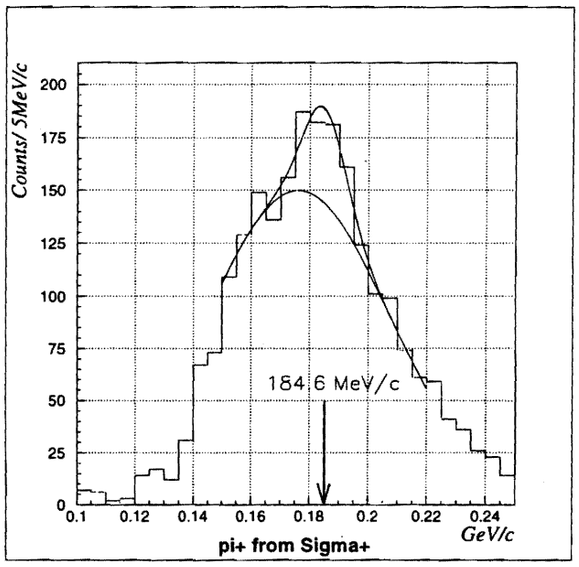

Figure 4.8: A histogram of the π^+ momentum from Σ^+ decay

4.2 Identification of Ξ^- Production

Even though the second-level trigger suppressed the contamination of knock out proton in KKCDH trigger on-line, the event rate of (K^-, K^+) reaction is only 3 % of the the acquired data. The K^+ events are selected at the off-line analysis based on the identification of the outgoing particle.

First, the data are processed with a simple tracking routine to analyze the momentum of the outgoing particles, and roughly select the reconstructed mass of the particle with information of time-of-flight between IT and BT. The data size is reduced to 1/20 and they are stored in a hard disk of the analysis computer. Secondly, events are further selected with a more precise tracking routine for better determination of the momentum and also for rejection of background events.

In the 1998 run, the primary protons were delivered to the production target with typically 7×10^{12} per spill. The accumulated number of K^-'s on the target was 0.9×10^{12} for about 800 effective beam hours. Among them, the number of (K^-, K^+) reactions was about 1.1×10^5.

4.2.1 Data Reduction

The events of Ξ^- production are purified by rejecting background events, which are originated from protons of (K^-, p) reaction and particles misidentified as K^+.

In the data reduction, a routine called PEANUT is used to determine the momentum of the outgoing particles, P_{out}. PEANUT is based on a first order transport theory. The transport matrices, which consist of partial derivatives of outgoing track

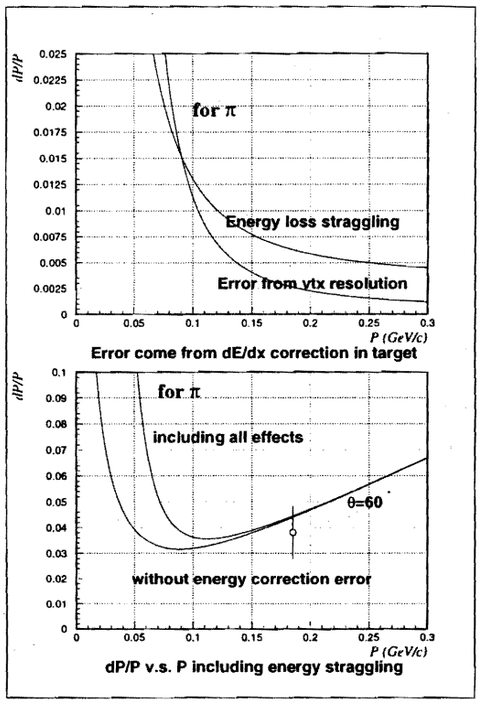

Figure 4.9: An estimation of the momentum resolution

parameters as functions of incoming track parameters, are prepared for each section of the spectrometer acceptance divided into 480. A track in a small region of phase space is approximated with a linear extrapolation from a central track in each section. A Monte Carlo simulation indicates that the error of the momentum obtained with this method is less than 0.3% of the true value.

Combining the analyzed momentum with the information of time-of-flight from the vertex of the (K^-, K^+) reaction to BT, TOF_{out}, the mass of the outgoing particles, $mass_{out}$, is reconstructed. Here the reaction vertices are determined by the hit of the drift chamber of upstream and downstream the target(ID1-3 and FD1-2). TOF from IT to the vertex, TOF_{ITvtx}, is calculated with the K^- momentum. A subtraction of the TOF_{ITvtx} from the measured TOF from IT to BT, TOF_{ITBT}, gives TOF_{out}.

$$TOF_{out} = TOF_{ITBT} - TOF_{ITvtx} \tag{4.1}$$

PEANUT also gives the path length of outgoing particle, $L_{pathout}$, then the beta, $beta_{out}$, was calculated.

$$beta_{out} = \frac{L_{pathout}}{TOF_{out} \times c} \tag{4.2}$$

Finally, the mass of the outgoing particle is given by,

Table 4.3: A summary of tracking efficiency

layer	3	4	6	7	9	P_{hit}	Eff_{track}	Eff
no missing						0.744	0.810	0.603
1 missing	x					7.2E-04	0.789	0.001
		x				3.8E-02	0.724	0.028
			x			1.0E-02	0.759	0.008
				x		4.9E-03	0.791	0.004
					x	5.9E-03	0.791	0.005
2 missing	x	x				3.7E-05	0.723	2.7E-05
	x		x			9.7E-06	0.735	7.1E-06
	x			x		4.7E-06	0.787	3.7E-06
	x				x	5.7E-06	0.784	4.5E-06
		x		x		2.5E-04	0.713	1.8E-04
		x			x	3.0E-04	0.713	2.2E-04
			x	x		6.6E-05	0.733	4.8E-05
			x		x	7.9E-05	0.741	5.9E-05
						0.805		0.647

$$mass_{out} = \frac{P_{out}}{beta_{out} \times \sqrt{1. - beta_{out}^2}} \tag{4.3}$$

The region 0.3 GeV/c^2 $\leq mass_{out} \leq$ 0.75 GeV/c^2 was selected for further analysis. We use the loose condition in this stage in order not to lose the data.

4.2.2 Data Selection

After the events is roughly selected and the data size is reduced in the first stage, we analyze the data more precisely for further rejection of background and a better determination of the momentum. We use a routine called WALNUT, which analyzes the momentum more precisely than PEANUT. It is based on the Runge-Kutta method, so that it takes more CPU time.

Fig 4.12 shows a plot of momentum vs. TOF for the outgoing particles. This shows that the K^+'s are clearly identified. Fig 4.13 shows a histogram of the mass of the outgoing particles. The cut condition is also shown in the figure, the events were selected in the region of 0.4 GeV/c^2 $\leq mass_{out} \leq$ 0.7 GeV/c^2.

Fig 4.13 is obtained using a part of data before the data reduction to emphasize the distribution of pions and protons. The contamination of misidentified pions or protons in the selected region was evaluated to be less than 1%. The contamination originated from the in-flight K^+ decay is estimated to be 3.7%. Therefore, the total background contamination in the selected K^+ events was estimated to be ~4%.

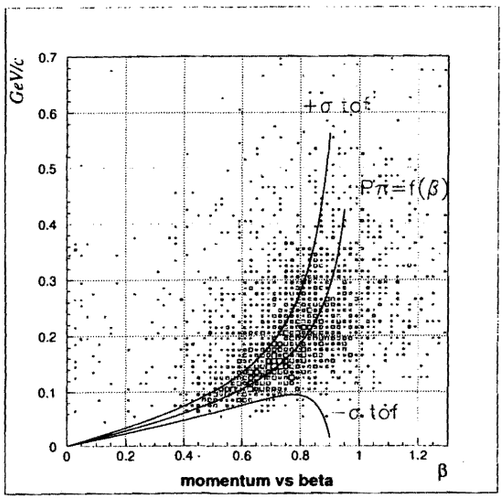

Figure 4.10: A plot of measured momentum vs. reconstructed beta with TOF information

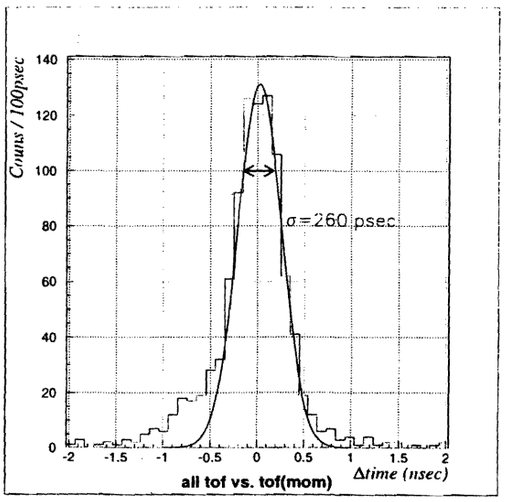

Figure 4.11: A histogram of the residual of the timing information between CDH and calculated timing.

We select the events, of which the (K^-, K^+) reaction vertex is in the target. The reaction vertices are reconstructed by the drift chambers upstream and downstream the target(ID1-3 and FC1-2).

Fig 4.14 shows a scatter plot of the vertex of (K^-, K^+) reaction and the projected histograms on x and y axes. The small bumps apparent on each side of the plot originate from the aluminum target installation bar. A box with a solid line in the figure shows the dimension of the target, which also presents a cut condition; $|X_{vtx}| \leq 2.54cm$ and $|Y_{vtx}| \leq 0.64cm$. A target cut in z direction is $|Z_{vtx}| \leq 50cm$, that is three times larger than the length of the target, taking into account of the z vertex resolution of 3.5 cm in sigma.

After selecting the good (K^-, K^+) events, the missing mass is reconstructed. Fig 4.15 shows a spectrum of the reconstructed missing mass assuming the $K^-p \rightarrow K^+X$. We see the peak of Ξ^- production around 1.321 GeV/c^2, which is smeared out by the Fermi momentum of ^{9}Be.

The amount of Ξ^-'s identified in the 1998 data is approximately 1.1×10^5. Sequential decaying two π^- is searched for among Ξ^- production events, the details are described in the next section.

4.3 Identification of $\Lambda\Lambda$ hypernuclei

In this section, I describe the way to identify $\Lambda\Lambda$ hypernuclei. First of all, the event which contains two π^-'s track in the CDS and the vertex of two π^-'s is in the target region are selected from the Ξ^- production events. Secondly, the events due to quasifree Ξ^- production are simulated by a Monte Carlo method.

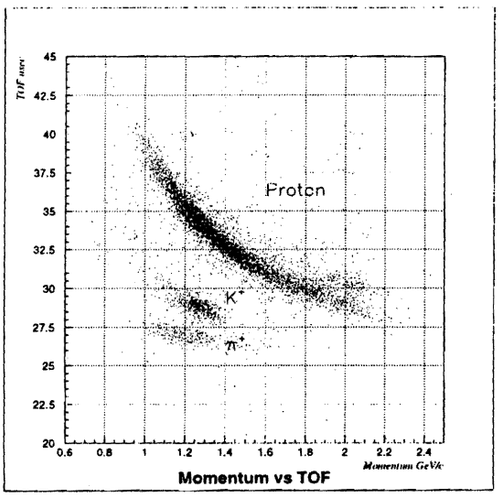

Figure 4.12: A scatter plot of TOF vs. momentum of the outgoing particles

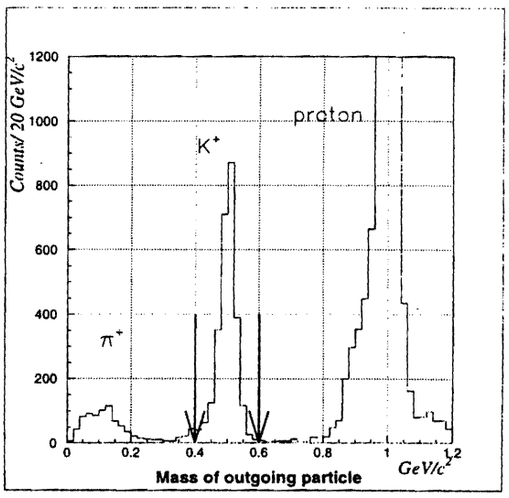

Figure 4.13: A histogram of the mass of the outgoing particles

The simulated results are tested by comparing some histograms with these derived from the acquired data. Thirdly, I search for the S=-2 nuclear system production and make an interpretation of the structure in the histograms. This leads to the identification of a hypernucleus; ${}^{4}_{\Lambda\Lambda}$H.

Note that, in this and the following section, "$\pi 1$" and "$\pi 2$" denotes the higher and lower momentum π^-, respectively.

4.3.1 Events of 2 π^- track in CDS

The criteria to select the $2\pi^-$ events are based on the vertex information and the particle identification.

As with the data of $p\pi^-$ elastic scattering, the vertex is assumed to be the center between two points which gives the closest distance(DCA) between two tracks projected on the X-Y plane. Fig 4.16 shows the histograms of 2 π^- vertex in x, y and z axis, where the solid lines show the target edge. The histogram in y axis shows the broad tail which likely comes from the Ξ^- free decay. The identified Ξ^- tends to go up and forward due to the K^+ acceptance, so that the vertex distribution in y axis seems to be shifted upward. The histogram of $2\pi^-$ vertex in z axis also seems to be shifted to a little bit forward.

Fig 4.17 shows a histogram of the distance between 2 points, DCA. The line in the figure shows the cut condition; $DCA \leq 2cm$.

A simulation to estimate the S/N ratio as a function of DCA has been performed.

Fig 4.18 gives the simulated DCA distribution of ΛΛ hypernuclei events, indicating that the events are concentrated in the region of less than 2 cm. The cut condition of DCA is chosen to be 2 cm, which corresponds to five times sigma of the vertex resolution, in order not to lose the events.

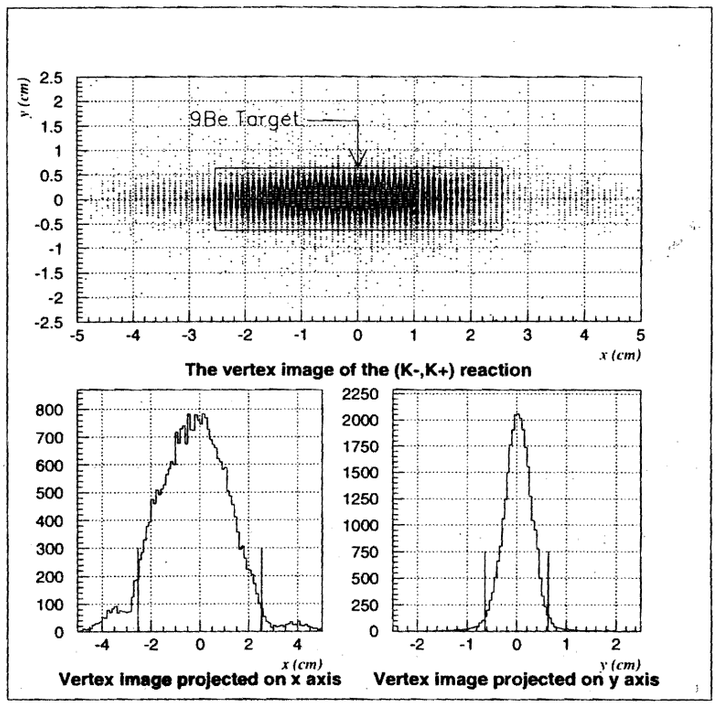

Figure 4.14: A scatter plot of the vertex of (K^-, K^+) reaction

Fig 4.19 shows the simulation result for the variation of signal percentage, background percentage and the S/N ratio as a function of DCA cut; circles show the survival percentage of the signal, stars show the survival percentage of Ξ^- free decay background and triangles show the ratio of signal to background in an arbitrary unit.

Fig 4.20 shows the scatter plots of analyzed momentum vs. reconstructed beta by TOF information, where the solid line shows the cut condition. The data is shifted toward a delayed timing, which is expected for the weak decay of $\Lambda\Lambda$ hypernuclei as well as the background Ξ^- decay. Hence the cut conditions are set to be asymmetric; δTOF's are $+2\sigma_{TOF}$ and $-\sigma_{TOF}$, respectively , where σ_{TOF} is 250 psec.

4.3.2 Monte-Carlo simulation for estimating the quasi-free Ξ^- decay background

The $2\pi^-$ events contain the π^-'s from the quasi-free Ξ^- decay. The quasi-free Ξ^-'s, which do not contribute to $\Lambda\Lambda$ conversion, decay and some of them leave 2 π^- tracks without proton track when the proton stops inside the target material and/or escapes from the CDS acceptance. A Monte-Carlo simulation was done in order to estimate the process. For the Ξ^- production in the (K^-, K^+) reaction, Fermi momentum distribution of proton in ^{9}Be is realistically treated [30]. The

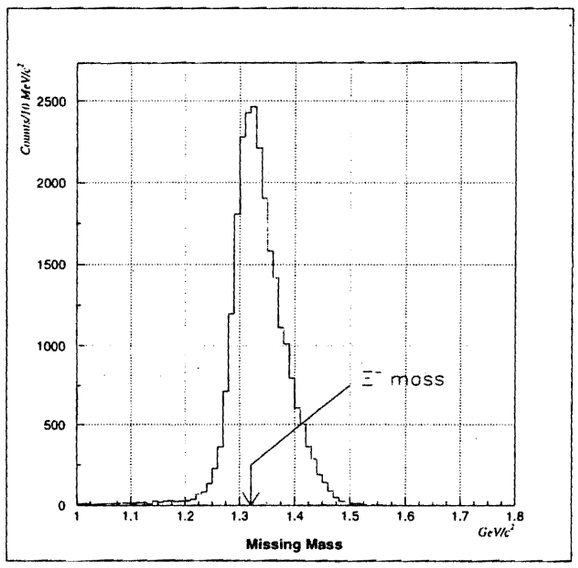

Figure 4.15: A spectrum of the missing mass

momentum distribution of K^- incident is also taken into account using the acquired data.

Fig 4.21 shows a simulated result of K^+ momentum in the (K^-, K^+) reaction, and the acquired data is also plotted. The simulated K^+ momentum distribution can reproduce the acquired K^+ histogram well.

Fig 4.22 shows simulated results of $2\pi^-$ momentum distributions of 3 track event, which consists of two π^-'s and one proton. The acquired π^-'s momentum distribution by the CDS is also plotted in the figure. Left-hand figure shows the π^-'s momentum distribution from Λ and right-hand figure shows the π^-'s momentum distribution from Ξ^-. These also show the good agreements each other.

Fig 4.23 shows a result of the simulation; a histogram of $\pi 1$ momentum where $\pi 2$ momentum is less than 110 MeV/c. The solid line presents a fitted result by a function; F(p).

$$F(p) = \sum_{i=0}^{6} A_i \times (p - 0.13)^i$$

The obtained background is normalized by the acquired number of $\Xi^-$by CDS.

CDS collects the Ξ^- events consisting of one positive and two negative tracks, which can reproduce the mass of Ξ^-. By comparing the number of Ξ^- events in the simulation data to the actually collected number of Ξ^- by CDS and taking into account the tracking efficiency, the simulated background level is absolutely normalized.

By definition, the following four equations are given.

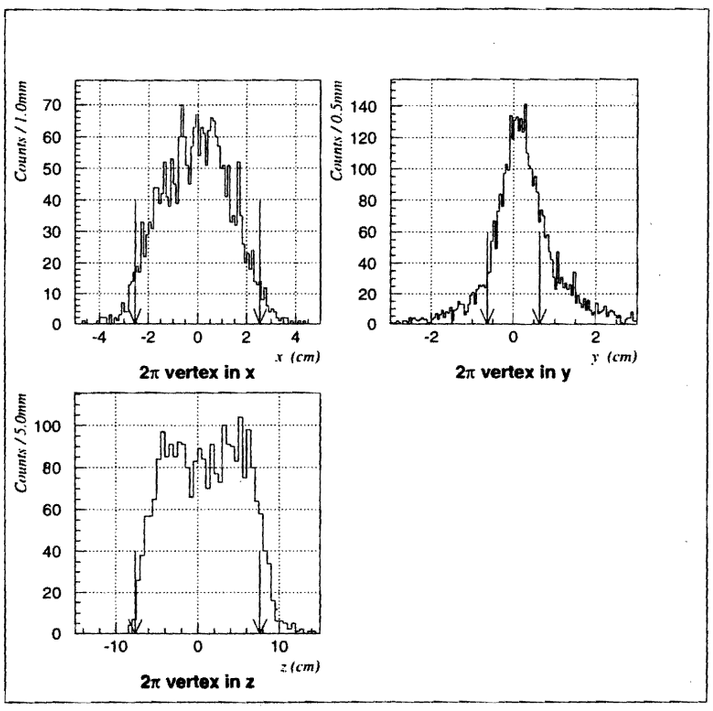

Figure 4.16: Histograms of the $2\pi^-$ vertex in x, y and z axes.

$$
\begin{aligned}
A_{sim\ \Xi} &= N_{sim\ \Xi} \\
A_{CDS\ \Xi} &= N_{CDS\ \Xi} \times Eff^2_{-track} \times Eff_{+track} \\
A_{sim\ 2\pi} &= N_{sim\ 2\pi} \\
A_{CDS\ 2\pi} &= N_{CDS\ 2\pi} \times Eff^2_{-track}
\end{aligned}
$$

$N_{CDS\ \Xi/2pi}$ and $A_{CDS\ \Xi/2pi}$ stand for the number of the each event in the CDS acceptance and the number of the events actually acquired, respectively. $N_{sim\ \Xi/2pi}$ and $A_{sim\ \Xi/2pi}$ mean the same for the simulated events. Eff_{-track} and Eff_{+track} are the tracking efficiencies of negative and positive track, respectively. These efficiencies are 65% independently of charges.

The equations, $N_{sim\ \Xi} = N_{CDS\ \Xi}$ and $N_{sim\ 2\pi} = N_{CDS\ 2\pi}$, finally lead $A_{CDS\ 2\pi}$ to the following relation;

$$
A_{CDS\ 2\pi} = \frac{1}{Eff_{+track}} \times \frac{A_{CDS\ \Xi}}{A_{sim\ \Xi}} \times A_{sim\ 2\pi}
$$

In the follwing analysis, the background level is always calculated using this formula.

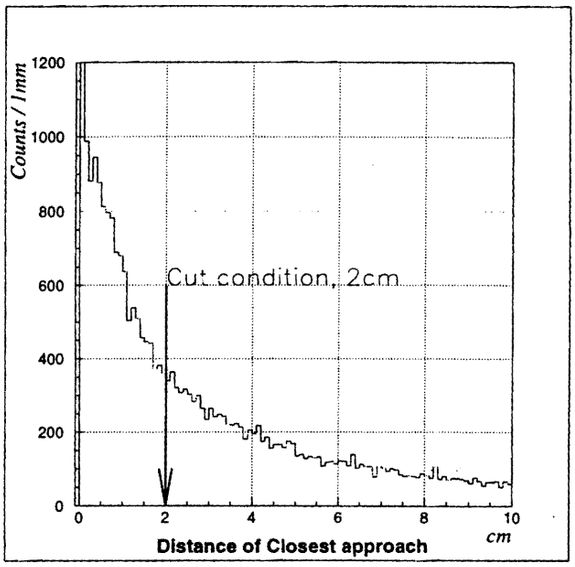

Figure 4.17: A histogram of the distance between 2 points.

The Ξ^-stopping rate is also estimated by the Monte-Carlo simulation, Fig 4.24 shows two histograms, the left figure is a histogram of kinetic energy distribution of Ξ^-, $e\Xi^-$, where the histogram of the stopped Ξ^- is overlaid and the right figure presents the stopping ratio of Ξ^- in the target as a function of $e\Xi^-$.

The total stopping ratio in this simulation is given to be 3.3 %, which is consistent with a result of experiment KEK-E224. This shows that the Ξ^-whose $e\Xi^-$ is larger than 100 MeV hardly stops in the target. When the event $e\Xi^- \leq 100$ MeV is selected, not only the stopped-Ξ^- process is enhanced but also the background from the quasi-free can be suppressed efficiently. In the following section, searching for the ΛΛ hypernuclei is done in a region of $e\Xi^- \leq 100$ MeV.

4.3.3 Searching for ΛΛ hypernuclei

In addition to the criteria which were described in the sub-section 4.3.1, we select the events with $E_{\Xi^-} \leq 100$ MeV for reason of the background suppression. A two dimensional plot of $\pi 1$'s momentum vs. $\pi 2$'s momentum from these events satisfying this requirement is shown in the Fig 4.25.

A $\pi 1$'s histogram, where the $\pi 2$ with less than 110 MeV/c is gated, is given in the Fig 4.26. The solid line is also shown in this figure which presents the estimated background from Ξ^- decay.

By overlaying the normalized background estimation on a $\pi 1$ histogram, some excess counts are observed. The excess counts are concentrated in the region from 90 to 140 MeV/c, where the decaying π^-'s from any hypernuclei are expected. The production of S=-2 nuclear system can be observed with our experimental principle.

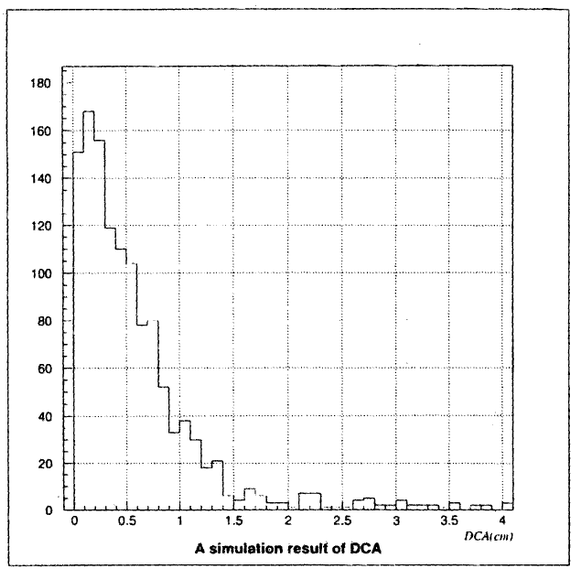

Figure 4.18: A histogram of the simulated distribution of DCA for ΛΛ hypernuclei event

This histogram shows at least three structures: one is from 100 to 110 MeV/c, another is from 110 to 125 MeV/c and the other is from 135 to 145 MeV/c. Here, I pay my attention to the most prominent structure from 110 to 125 MeV/c and try to give an explanation of it. The rest will be discussed in the following Chapter 5.

We also see the $\pi 2$ histogram, where the $\pi 1$ momentum between 110 and 125 MeV/c is gated. Fig 4.27 shows the $\pi 2$ histogram and the background level. This also shows the large excess counts over the background.

Recalling what we are studying, they are the events which are in the region presented by the box in the Fig 4.25; $\pi 1$ are between 110 and 125 MeV/c and $\pi 2$ are between 85 and 110 MeV/c. Assuming $^{9}\mathrm{Be} + \Xi^{-} \rightarrow {}^{10}_{\Lambda\Lambda}\mathrm{Li}^{*}$ reaction of the stopped Ξ^{-}process, Table 4.4 shows a summary of what kinds of hypernuclei we can expect in this region. Concerning the direct process discussed in Chapter 1, there are no candidates for twin single-Λ hypernuclei in this region.

$\pi 1$ histogram

The structure of $\pi 1$ in the Fig 4.26 possibly contains three kinds of π^{-}; 114.3 MeV/c from ${}^{3}_{\Lambda}\mathrm{H}$, ~116 MeV/c from ${}^{4}_{\Lambda\Lambda}\mathrm{H}$ and ~ 117 MeV/c from ${}^{9}_{\Lambda\Lambda}\mathrm{Li}$. Here, the momentum with "~" are the expectations by a calculation. The momentum resolution in this region is about 4 MeV/c in sigma which is given by the study of the momentum resolution in the last section. I try to fit this structure between 109 and 124 MeV/c by Gaussian fitting with a fixed width of 4 MeV/c and Fig 4.28 shows the results.

The left-hand side of Fig 4.29 shows the fitting of the $\pi 1$ peak with a single Gaussian whose centroid is 114.3 MeV/c and width is 4 MeV/c. It gives a result of

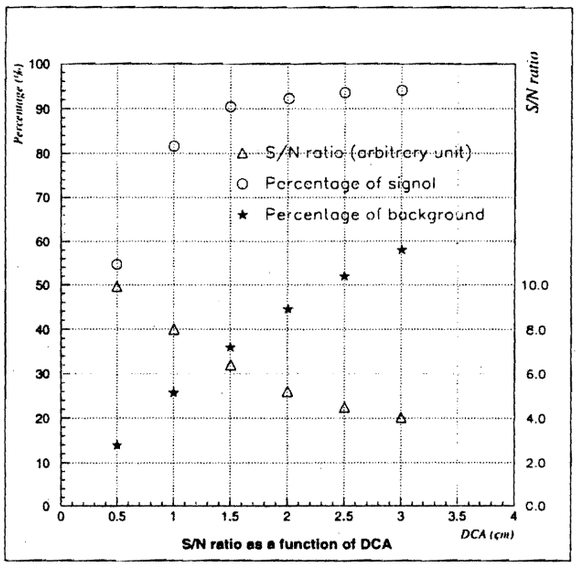

Figure 4.19: A plot of the simulation result; circles show the survival percentage of the ΛΛ events as a function of DCA, stars the survival percentage of Ξ^- free decay background and triangles the ratio of signal to background in an arbitrary unit.

χ^2/Ndof to be 8.024/5, which is expected to be about 20% CL. The right-hand side of Fig 4.28 shows the fitting with two Gaussians, whose centroid are 114.3 and 117.0 MeV/c and widths are 4 MeV/c for each, respectively. It gives a result of χ^2/Ndof to be 1.077/4, which is expected to be about 90% CL. It is more likely that the peak consists of two peaks rather than one single peak, that is, this peak may contain the π^- from ΛΛ hypernuclei.

$\pi 2$ histogram

The $\pi 2$ histogram shows a more complicated structure. The species of the possible hypernuclei in Fig 4.27 are five and some of them decay into three body.

Concerning the twin single Λ hypernuclei, only two cases are possible;

$$\begin{aligned} {}^{10}_{\Lambda\Lambda}\mathrm{Li}^* &\rightarrow {}^{6}_{\Lambda}\mathrm{He} + {}^{3}_{\Lambda}\mathrm{H} + \mathrm{n}(\mathrm{Q} = 4.2\mathrm{MeV}) \\ &\rightarrow {}^{5}_{\Lambda}\mathrm{He} + {}^{3}_{\Lambda}\mathrm{H} + 2\mathrm{n}(\mathrm{Q} = 4.0\mathrm{MeV}) \end{aligned}$$

when the $\pi 1$ momentum is between 110 and 125 MeV/c. The phase space volume of the final states for the small Q value is proportional to $(Q/\hbar\omega)^{(3n-5)/2}$ for n-body breakup, where $\hbar\omega$=21.6MeV is the oscillator strength of the nucleus [33]. This gives the ratio of the formation rate of ${}^{6}_{\Lambda}$He to ${}^{5}_{\Lambda}$He as 14 to 1. Furthermore, the escaping neutron is p-wave. According to this, it is reasonable to ignore the contribution of ${}^{5}_{\Lambda}$He.

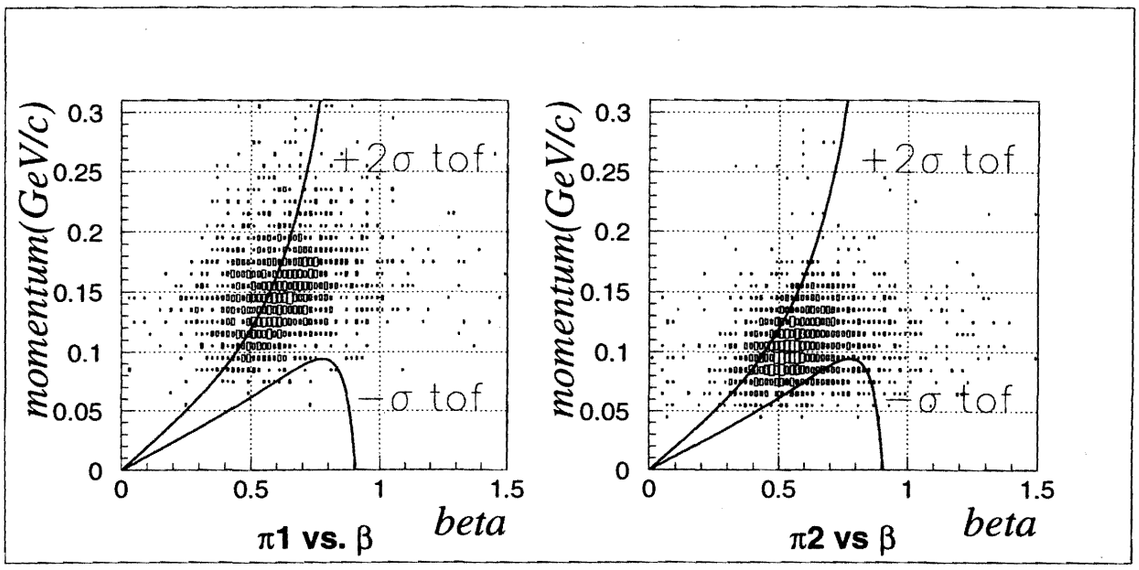

Figure 4.20: Plots show the analyzed momentum vs. reconstructed beta of each π^-

${}^{9}_{\Lambda}$Be, which is the daughter nucleus of ${}^{9}_{\Lambda\Lambda}$Li, decays into two body, so that the π^- of 97.0 MeV/c should appear as a peak structure. In the Fig 4.27, the feature in the region less than 100 MeV/c shows a broad tail down to the lower momentum instead of a peak structure around 97.0 MeV/c. It seems to be composed of any three body decay. The apparent lack of a two-body peak is interpreted as indicating a negligible production of ${}^{9}_{\Lambda}$Be, ${}^{9}_{\Lambda\Lambda}$Li.

Now, $\pi 2$ histogram is also studied by fitting with the three or two components. As I mentioned in the Chapter 1, the π^-'s momentum histogram into three body decay from ${}^{4}_{\Lambda}$He has been studied well. The fitting function for ${}^{4}_{\Lambda}$He decay is constructed by using the theoretical calculation in Fig 1.2 with smearing by the CDS resolution.

The left-hand histogram in Fig 4.29 shows the result by assuming only two components; ${}^{4}_{\Lambda}$He and ${}^{6}_{\Lambda}$He. It gives a result of χ^2/Ndof to be 6.167/11, which is expected to be less than 90% CL. The right-hand figure shows the result by assuming the third component in addition to ${}^{4}_{\Lambda}$He and ${}^{6}_{\Lambda}$He. It gives a result of χ^2/Ndof to be 4.238/10, which is expected to be about 95% CL. The fitted region is between 80 and 116 MeV/c in both of figure. It should be noticed that the yield around 100 MeV/c cannot be reproduced well without this third component. I assumed the third component to be a Gaussian whose centroid is 103 MeV/c and width is 3.7 MeV/c in sigma, respectively. It should be stressed that π^- momentum from any single-Λ hypernuclei cannot account for this component and that the decay from double-Λ hypernuclei is the most probable explanation. This will correspond to the three body decay of ${}^{4}_{\Lambda\Lambda}$H, but any calculation of the π^- momentum from ${}^{4}_{\Lambda\Lambda}$H into three body decay has not been published.

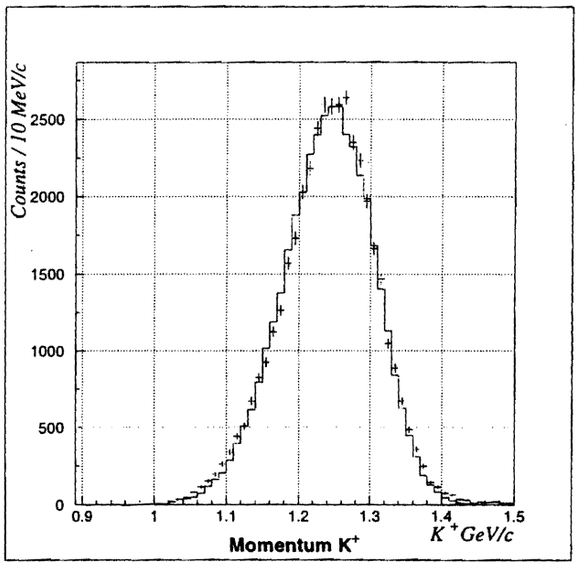

Figure 4.21: A simulation result of K^+ momentum in the (K^-, K^+) reaction. The acquired data is also plotted.

${}^{4}_{\Lambda\Lambda}$H hypernuclei

Based on the study by fitting the histograms, it is difficult to understand the $\pi 1$ and $\pi 2$ spectra without assuming the sequential decay mode of ${}^{4}_{\Lambda\Lambda}$H, ${}^{4}_{\Lambda\Lambda}\mathrm{H} \rightarrow {}^{4}_{\Lambda}\mathrm{He} + \pi^-$, ${}^{4}_{\Lambda}\mathrm{He} \rightarrow {}^{3}\mathrm{He} + \mathrm{p} + \pi^-$and ${}^{4}_{\Lambda\Lambda}\mathrm{H} \rightarrow {}^{3}_{\Lambda}\mathrm{H} + \mathrm{p} + \pi^-$, ${}^{3}_{\Lambda}\mathrm{H} \rightarrow {}^{3}\mathrm{He} + \pi^-$.

To obtain the quantitative information on the binding energy of ${}^{4}_{\Lambda\Lambda}$H, a $\pi 1$ histogram is made by gating the π^- from ${}^{4}_{\Lambda}$He; $\pi 2$ between 85 and 100 MeV/c. Fig 4.30 shows the histogram and the result of the fitting between 109 and 124 MeV/c by a single Gaussian. The peak position and the width are 116.4±1.4 MeV/c and 4.6±1.7 MeV/c, respectively.

The width is consistent with our estimation of the momentum resolution. The π^- momentum from ${}^{4}_{\Lambda\Lambda}$H is given to be 116.4±1.4(stat.)±1.2(syst.)(MeV/c).

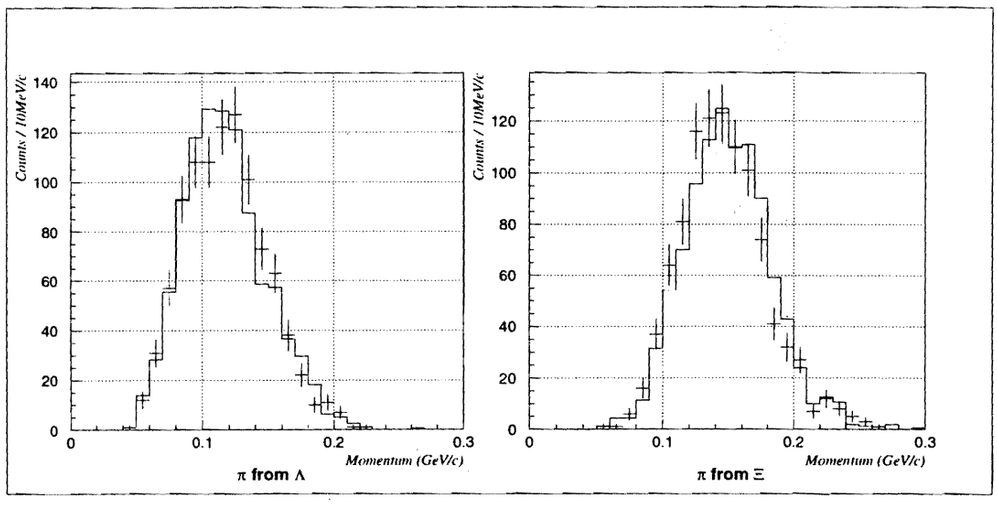

Figure 4.22: Simulated results of $\pi 1$ and $\pi 2$ momentum distribution of three track event, and the acquired π^-'s momentum distribution is also plotted.

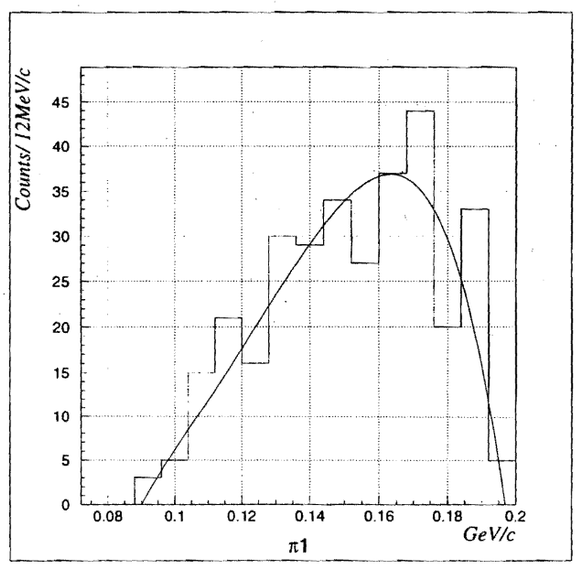

Figure 4.23: A simulation results of $\pi 1$ momentum where $\pi 2$ momentum with less than 110 MeV/c is gated.

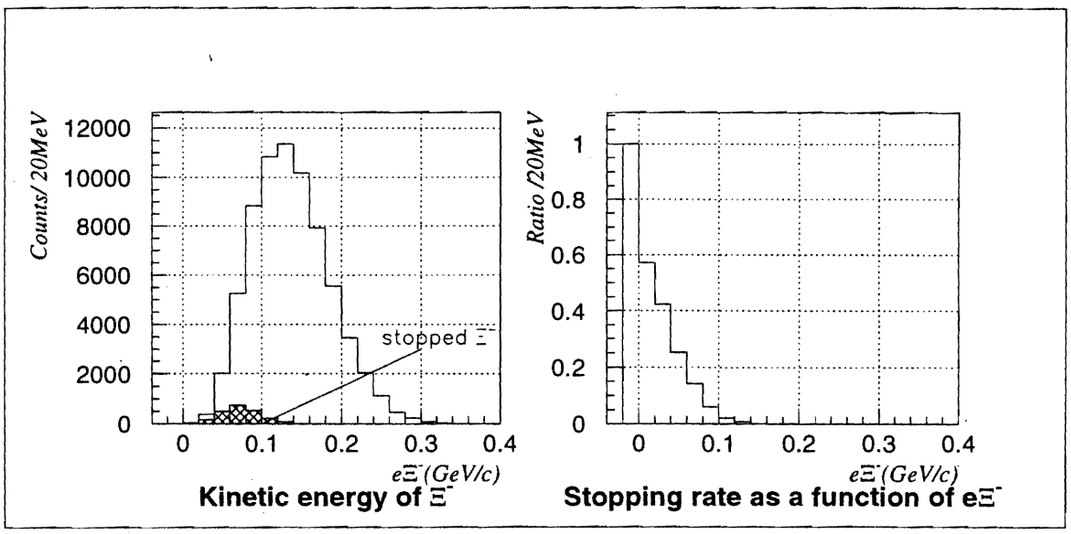

Figure 4.24: A simulation result; the left-hand figure shows the histogram of kinetic energy distribution of $\Xi^-(e\Xi^-)$ and the histogram of the stopped Ξ^-. The right-hand figure shows the stopping rate as a function of $e\Xi^-$.

Table 4.4: A table of S=-2 nuclear system that can be expected in the region, $\pi 1$ are between 110 to 125 MeV/c and $\pi 2$ are less than 110 MeV/c.

	$\pi 1$		$\pi 2$	
ΛΛhypernuclei	${}^{4}_{\Lambda\Lambda}$H	∼116	${}^{4}_{\Lambda}$He	∼96.0(3-body)
	${}^{3}_{\Lambda}$H	114.3	${}^{4}_{\Lambda\Lambda}$H	∼106(3-body)
	${}^{9}_{\Lambda\Lambda}$Li	∼117	${}^{9}_{\Lambda}$Be	97.0
Twin single Λhypernuclei	${}^{3}_{\Lambda}$H	114.3	${}^{5}_{\Lambda}$He	∼99.2(3-body)
	${}^{3}_{\Lambda}$H	114.3	${}^{6}_{\Lambda}$He	108.4

Note1: The momenta of ΛΛ hypernuclei with "∼"are derived by theoretical calculations [31] and [32], which try to reproduce the $B_{\Lambda\Lambda}$ of the old emulsion data.
Note2: The three body decay of ${}^{4}_{\Lambda\Lambda}$H has not been studied theoretically, yet. This shows the momentum of end-point of three body decay.
Note3: The ${}^{4}_{\Lambda\Lambda}$H is considered to decay mainly to ${}^{4}_{\Lambda}$He*(Ex=1.15 MeV) due to the dominance of the spin non-flip amplitude in the pionic weak decay.

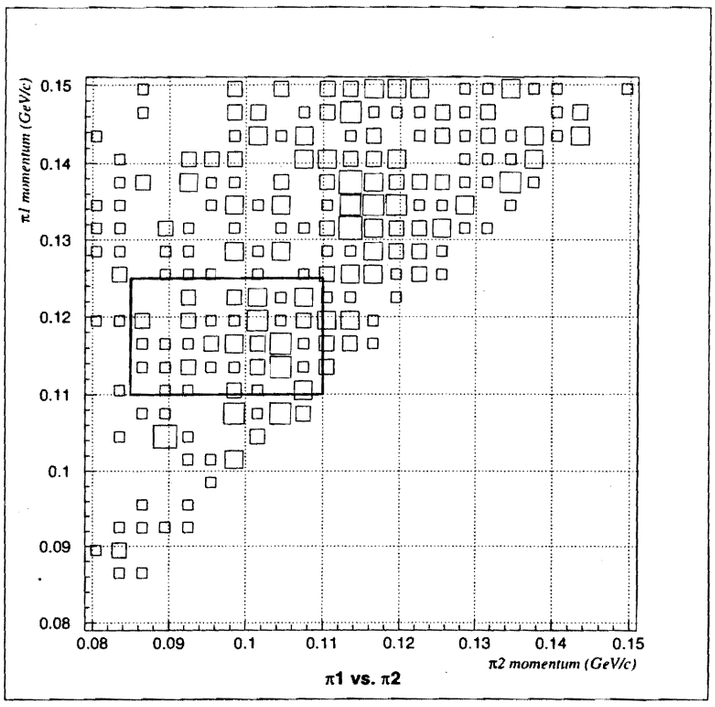

Figure 4.25: A momentum plot of $\pi 1$ vs. $\pi 2$. The square box in the figure shows the region, $\pi 1$ are between 110 and 125 MeV/c and $\pi 2$ are between 85 and 110 MeV/c, where we are going to search for the $\Lambda\Lambda$ hypernuclei.

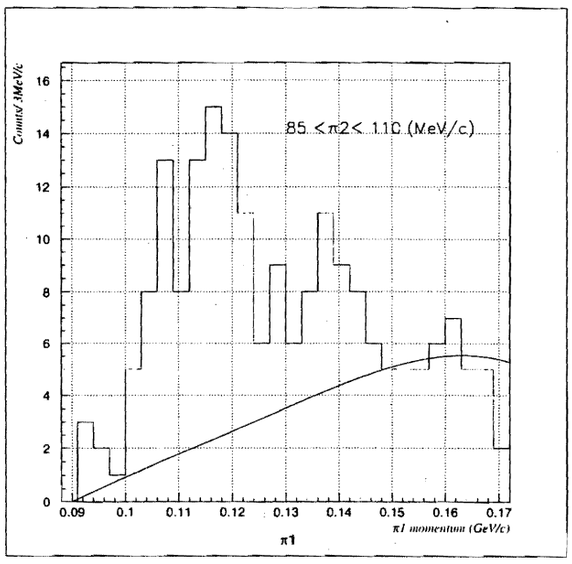

Figure 4.26: A histogram of $\pi 1$ where $\pi 2$ less than 110 MeV/c is gated.

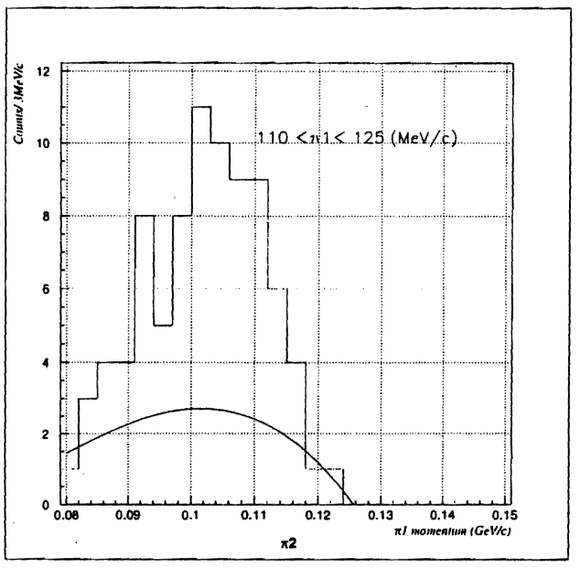

Figure 4.27: A histogram of $\pi 2$ where $\pi 1$ between 110 and 125 MeV/c is gated.

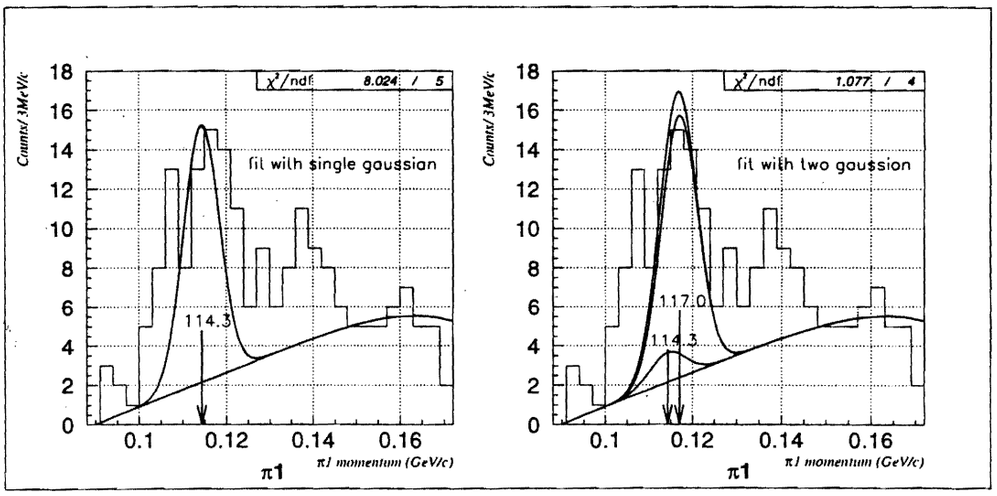

Figure 4.28: The result of a test by fitting $\pi 1$ histogram; the left-hand figure shows the result with the single Gaussian, and right-hand figure shows the result with the two Gaussians. The fitted region is between 109 and 124 MeV/c.

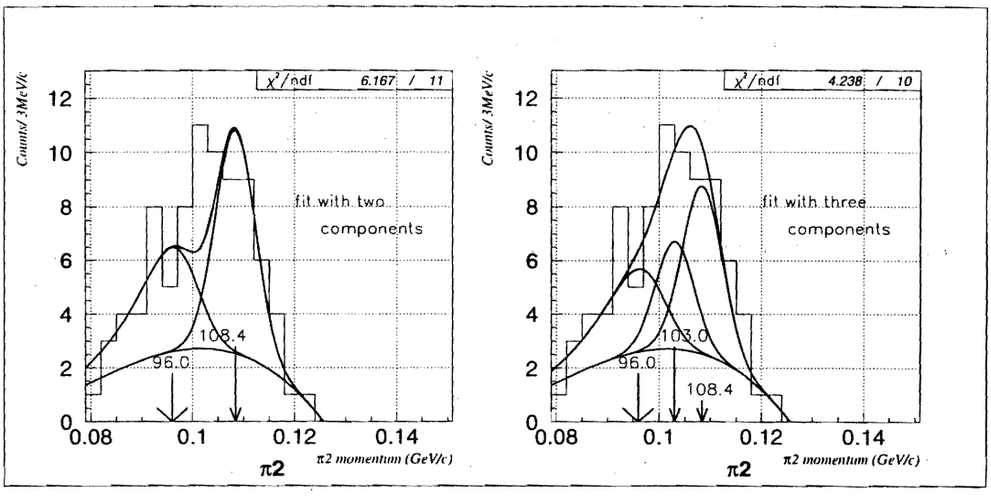

Figure 4.29: The result of a test by fitting $\pi 2$ histogram; the left-hand figure shows the result by assuming the contribution from ${}^{4}_{\Lambda}$He and ${}^{6}_{\Lambda}$He, the right-hand figure shows the result by assuming the third component in addition to ${}^{4}_{\Lambda}$He and ${}^{6}_{\Lambda}$He. The fitted region is between 80 and 116 MeV/c.

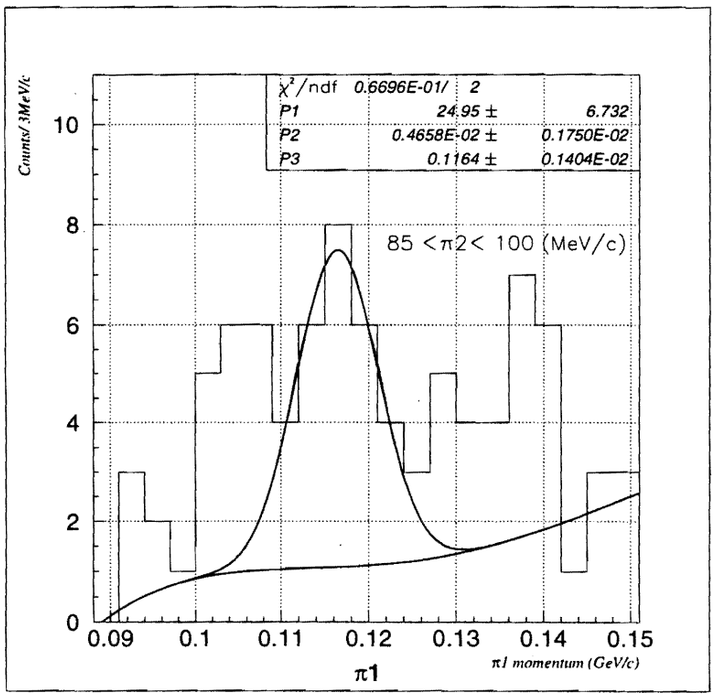

Figure 4.30: A histogram of $\pi 1$ where $\pi 2$ between 85 and 100 MeV/c is gated. The solid line presents the result of a Gaussian fitting. The fitted region is between 109 and 124 MeV/c.

Chapter 5

Results and discussion

5.1 Details of the $2\pi^-$ events close to the ${}^{4}_{\Lambda\Lambda}$H signal

In the previous chapter, I have demonstrated that the sequential decay of ${}^{4}_{\Lambda\Lambda}$H is observed in the region of $\pi 1$ momentum with 110 - 125 MeV/c and $\pi 2$ momentum with 85 - 110 MeV/c. In this section, I try to identify the other 2 π^- events close to the ${}^{4}_{\Lambda\Lambda}$H signal and discuss the significance of the ${}^{4}_{\Lambda\Lambda}$H signal.

The two-dimmensional histogram is inspected more closely in this section in order to study $\Lambda\Lambda$ hypernuclei quantitatively.

5.1.1 Overview of the 2 π^- histogram

The S=-2 nuclear system are classified into three categories according to the final state to which $\Lambda\Lambda$ compound state breaks up. The first is one free Λ process, which consists of a free Λ and a single-lambda hypernucleus. Around the region of ${}^{4}_{\Lambda\Lambda}$H concerned, possible species of this category are ${}^{9}_{\Lambda}$Li+Λ, ${}^{8}_{\Lambda}$He+Λ, ${}^{7}_{\Lambda}$He+Λ, ${}^{7}_{\Lambda}$Li+Λ and ${}^{6}_{\Lambda}$He+Λ. (see Fig A.1) The second is the twin single-Λ hypernuclear production. In this case, a combination of ${}^{6}_{\Lambda}$He and ${}^{3}_{\Lambda}$H is possible. The third is $\Lambda\Lambda$ hypernuclei production. It includes ${}^{4}_{\Lambda\Lambda}$H which we are interesting in. Other kinds of $\Lambda\Lambda$ hypernuclei are also possible.

Fig 5.1 is a $\pi 1$ vs. $\pi 2$ scatter plot, where the posible origins of the $2\pi^-$ events are schematically shown.

In the case of one free Λ process, a free Λ has a recoil momentum and decays in-flight due to the Q value originating from Ξ^- conversion, $\Xi^-p \rightarrow \Lambda\Lambda$, so that the momentum of the decaying $\pi^-$from the free Λ is widely spread. Moreover, the reconstructed vertex between 2 π^- track will deviate from the real vertex point due to decay in-flight, which affects the energy loss correction in the target and results in spread for both π^- momenta.

Monte-Carlo simulations to estimate the momentum histogram of π^- from free Λ are performed in the same cut condition of the $2\pi^-$ events. The π^- histograms

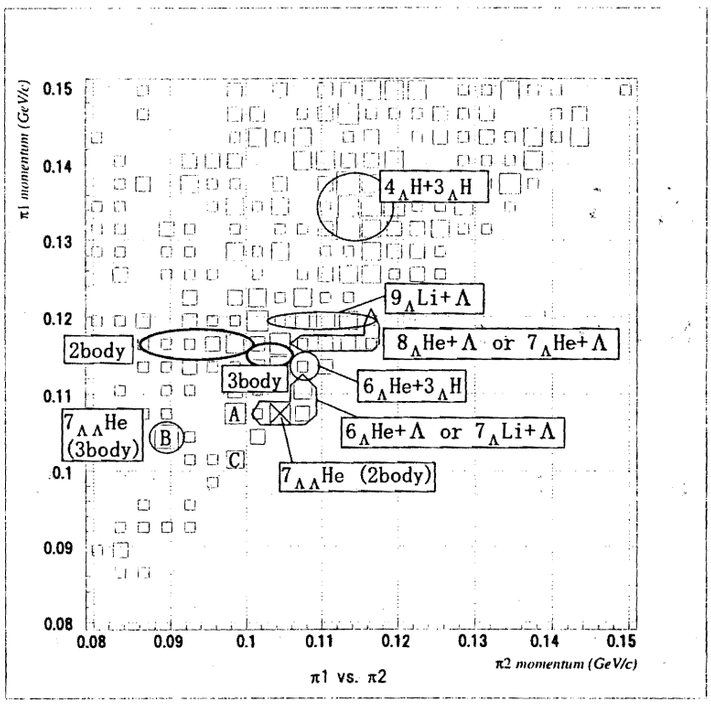

Figure 5.1: A momentum plot of $\pi 1$ vs. $\pi 2$ and possible origins of the $2\pi^-$ events.

show the structure whose peak is located higher than 110 MeV/c and whose yield is concentrated in the region higher than 100 MeV/c. It turns out that the total counts in the signal region, between 90 MeV/c and 100 MeV/c, is less than one third of the count in the region between 110 and 120 MeV/c. The number of single Λ process in the region where $\pi 1$ momentum is between 110 and 120 MeV/c and $\pi 2$ momentum between 115 and 121 MeV/c is less than eight counts. Therefore the contamination of one free Λ process to the signal region between 90 MeV/c and 100 MeV/c is less than two counts, which is less than 10% of the signal (25 counts from Fig 4.30).

A possible combination of twin single-Λ hypernucleus is ${}^{6}_{\Lambda}$He and ${}^{3}_{\Lambda}$H. The expected region of the combination is circled in Fig 5.1, and this shows only a few counts in the circle. It can be said that the production rate of twin single-Λ hypernuclei is relatively low.

The 2 π^- data shows a sign of another candidate of the $\Lambda\Lambda$ hypernuclei, ${}^{7}_{\Lambda\Lambda}$He, even though it is hard to confirm the existence due to the statistics. The momentum of π^- decays from ${}^{7}_{\Lambda\Lambda}$He is exepcted to be about 104 $\sim$ 105 MeV/c. The daughter nucleus of ${}^{7}_{\Lambda\Lambda}$He, ${}^{7}_{\Lambda}$Li undergoes two kinds of decay mode; one is the 2-body decay where the momentum of π^- is 108.1 MeV/c and the other is the 3-body decay where the momenutm of π^- is 90.0 MeV/c. In the Fig 5.1, the possible events are marked; the 3-body candidate with circle and the 2-body candidate with X.

5.1.2 Signal significance

In this subsection, significance of the ${}^{4}_{\Lambda\Lambda}$H signal is studied based on the consideration in the previous subsection.

The events in the region of $\pi 1$ momentum less than 110 MeV/c and $\pi 2$ momentum less than 100 MeV/c can contain other contributions which contaminate the signal. In Fig 5.1, regions of relatively large event density are marked with A, B, and C. One can consider that A is the tail of the one free Λ process, but the count is too much for the lower edge of the tail. B can be regarded as a candidate of ${}^{7}_{\Lambda\Lambda}$He with three body decay. No interpretation is given for the coponent C. Assuming these A, B and C come from the different origins, the $\pi 1$ structure between 100 MeV/c and 110 MeV/c in Fig 4.30 is fitted by the function, which is composed of three Gaussians. Counts leaking in from the parasitic species are considerd as the tail of the fitted function.

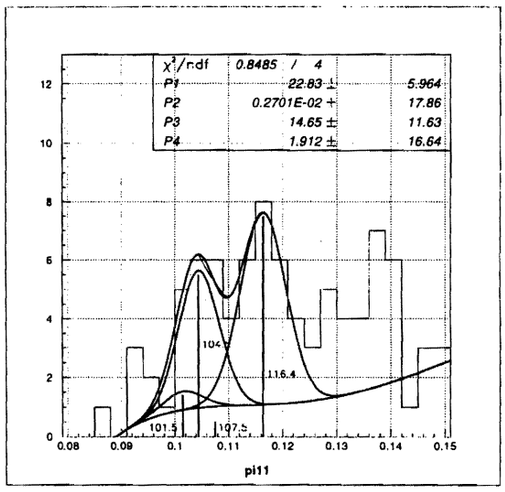

Figure 5.2: A histogram of $\pi 1$ where the $\pi 2$ is between 85 and 100 MeV/c. The solid lines show the fitted result with a function which is composed of three Gaussians representing parasitic components, and a Gaussian representing the signal. The fitted region is between 105 and 124 MeV/c.

Fig 5.2 shows a result of fitting for the region between 105 and 124 MeV/c with a function of 3 components Gaussian and a Gaussian for the signal, where the centroids of Gaussian are 107.5, 104.5 and 101.5 MeV/c for the lower momentum events and the centroid for the signal is 116.4 MeV/c, respectively. The widths of them are fixed to be 3.6% of the centroid. This assigns a negligibly small contribution to component A at a centroid of 107.5 MeV/c. Even though the trials of fitting are performed with varying the centroid for the componets A from 106 to 109 MeV/c, the peak count is almost negligible. It might be considered that the component A is a statistical fluctuation of the background.

According to the fitting result, the leakage from B totals 3.4 ± 2.7, from C is 0.1 ± 0.7. The total leakage count is 3.5 ± 2.8. Accordingly, the signal count is obtained to be 22.8±6.0. This is significantly large as compared to the square root of the background counts between 103 and 130 MeV/c; $\sqrt{9.0} = 3.0$. Therefore the peak of ${}^{4}_{\Lambda\Lambda}$H is confirmed to have a statistical siginificance.

I study how the $\pi 1$ momentum histogram, where $\pi 2$ between 85 and 100 MeV/c is gated, depends on the choice of the histogram; the width of bins and the position of bin edges.

Fig 5.3 shows the histogram, whose width of bins is events/2 MeV/c. The solid line shows the fitted curve where the background is normalized for this bin condition. This shows the centroid of the ${}^{4}_{\Lambda\Lambda}$H peak agrees with the result in Fig 4.30 within a sigma and the width is consistent with the expected resolution.

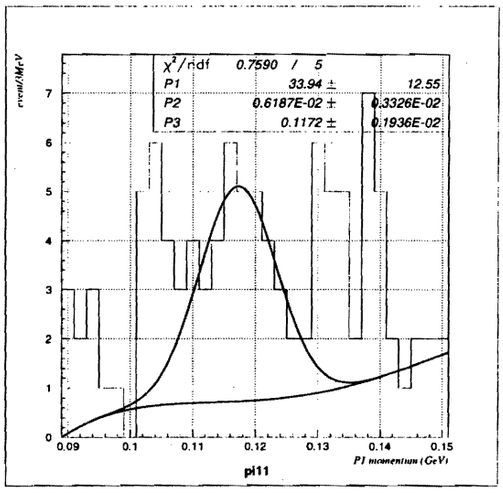

Figure 5.3: The histogram of $\pi 1$ momentum with the same cut conditon as Fig 4.30, where the width of histogram bin are 2MeV/c. The solid line shows the result of fitting.

Fig 5.4 shows the histogram whose edge of bins are shifted by 1.5 MeV/c from the edges in Fig 4.30. This also shows the centroid of the fitted peak agrees with the result in Fig 4.30 within a sigma and the width is consistent with the expected resolution.

The observed spectra and the resulting fits were shown to be insensitive to rebinning. The same results were obtained within statistical uncertainties.

I also study the dependence on the momentum cut condition. Fig 5.5 shows a histogram of $\pi 1$ momentum where $\pi 2$ between 85 and 96 MeV/c is gated. Fig 5.6 shows a histogram of $\pi 1$ momentum where $\pi 2$ between 85 and 104 MeV/c is gated.

The overall feature of the histograms is not so much changed and the fitting results agree with the result in Fig 4.30, although the low statistics or the contamination from other processes may obscure the signal.

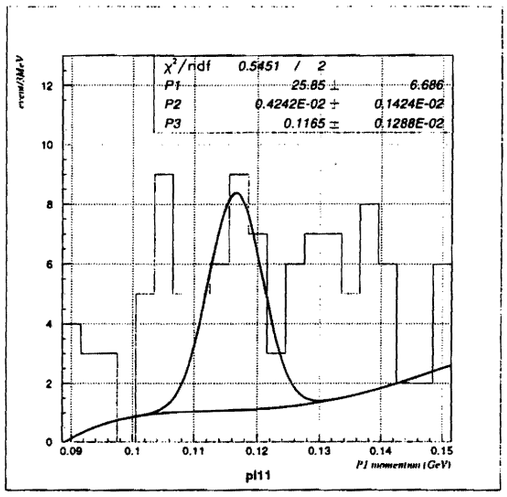

Figure 5.4: The histogram of $\pi 1$ momentum with the same cut condition as Fig 4.30, where the edges of histogram bin is shifted by 1.5 MeV/c from the edges of Fig 4.30. The solid line shows the result of fitting.

5.2 ${}^{4}_{\Lambda\Lambda}$H

We obtained the π^- momentum of ${}^{4}_{\Lambda\Lambda}$H $\rightarrow {}^{4}_{\Lambda}$ He+π^- to be 116.4±1.4(stat.)±1.2(syst.) MeV/c. The spin-parity of ${}^{4}_{\Lambda\Lambda}$H is considered to be $S^p = 1^+$, so that ${}^{4}_{\Lambda\Lambda}$H will mainly decay into the excited state of ${}^{4}_{\Lambda}$He* (Ex = 1.15 MeV, $S^p = 1^+$) because of the dominance of the non spin-flip amplitude in the mesonic decay [34]. Assuming this, a ${}^{4}_{\Lambda\Lambda}$H mass of 4106.2 ±0.94(stat.)±0.80(syst.) MeV is deduced. It corresponds to a $\Lambda\Lambda$ bond energy $\Delta B_{\Lambda\Lambda}$ of 0.47 ±0.94(stat.)±0.80(syst.) MeV. Even though the $\Delta B_{\Lambda\Lambda}$ includes zero within error, the existence of ${}^{4}_{\Lambda\Lambda}$H means that the $\Lambda\Lambda$ interaction is attractive.

It is important to give an evidence of the ${}^{4}_{\Lambda\Lambda}$H because the ${}^{4}_{\Lambda\Lambda}$H is expected to be marginally bound and gives a stringent limit for the $\Lambda\Lambda$ force. Theorists have been discussing the existence of the lightest $\Lambda\Lambda$ hypernucleus, ${}^{4}_{\Lambda\Lambda}$H. As a playground of the study of the baryon-baryon interaction, theorists tried to fit the experimental data, ${}^{10}_{\Lambda\Lambda}$Be, ${}^{6}_{\Lambda\Lambda}$He and ${}^{5}_{\Lambda}$He by taking into account $\alpha - \Lambda$ potential as well. This treatment did not predict the ${}^{4}_{\Lambda\Lambda}$H existence and gave an inconsistent strength of the Λ-Λ interaction deduced from the ${}^{6}_{\Lambda\Lambda}$He and ${}^{10}_{\Lambda\Lambda}$Be data; the former give a pretty large attractive force. Later on, the importance of $\alpha\alpha\Lambda$ potential was pointed out and it was introduced to fit the ${}^{9}_{\Lambda}$Be data, but a calculation still denied the existence of ${}^{4}_{\Lambda\Lambda}$H. Nakaichi and Akaishi claimed that $\alpha\Lambda\Lambda$ should be also considered to treat ${}^{10}_{\Lambda\Lambda}$Be data more precisely [31]. In their treatment, consistency among the $B_\Lambda({}^{5}_{\Lambda}\mathrm{He})$, $B_\Lambda({}^{9}_{\Lambda}\mathrm{Be})$ and $B_{\Lambda\Lambda}({}^{10}_{\Lambda\Lambda}\mathrm{Be})$ can be obtained and ${}^{4}_{\Lambda\Lambda}$H is bound by 0.3 MeV. A repulsive nature of 3 body potential makes the effective Λ-Λ strength larger. In any case, the existence of ${}^{4}_{\Lambda\Lambda}$H requires an attractive interaction between Λ's. Our result gives a

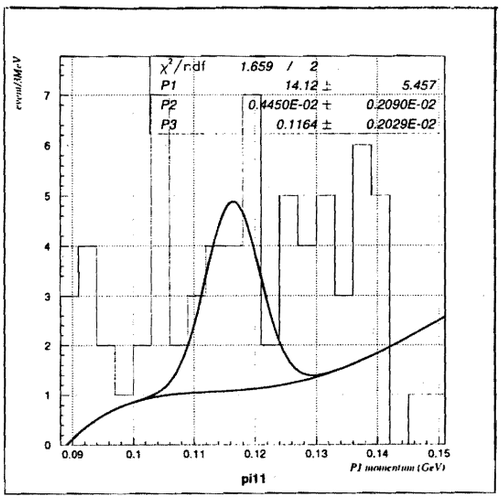

Figure 5.5: $\pi 1$ histogram, where $\pi 2$ between 85 and 96 MeV/c is gated. The solid line shows the fitting result.

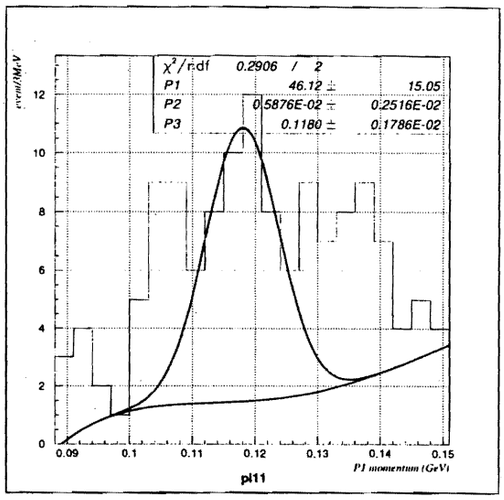

Figure 5.6: $\pi 1$ histogram, where $\pi 2$ between 85 and 104 MeV/c is gated. The solid line shows the fitting result.

binding, 0.6 MeV±0.94(stat.)±0.80(syst.), which is consistent with their estimation.

On the other hand, the existence of ${}^{4}_{\Lambda\Lambda}$H gives us the lowest limit of the mass of H-particle, M_H, because ${}^{4}_{\Lambda\Lambda}$H is the least bound system with S=-2. As $M_H > 2M_\Lambda - B_{\Lambda\Lambda} = M({}^{4}_{\Lambda\Lambda}H) - M({}^{2}H)$, the present experiment gives the lower limit of M_H to be 2230.6 ±0.94(stat.)±0.80(syst.)(MeV).

5.3 Formation of S=-2 system from ${}^{10}_{\Lambda\Lambda}$Li*

I will discuss the formation of S=-2 system from ^{9}Be+Ξ^- $\rightarrow {}^{10}_{\Lambda\Lambda}$ Li* reaction (stopped Ξ^- process).

The 2 body final state, ${}^{9}_{\Lambda\Lambda}$Li+n, has the largest Q value of 28 MeV among the possible final states. A large Q value gives a large phase space in the final state, but our data shows that the formation of ${}^{9}_{\Lambda\Lambda}$Li, as it was discussed in the last section, is not very large. This suggests that the formation rate does not simply depend on the phase space.

The final states giving the ${}^{4}_{\Lambda\Lambda}$H are ${}^{4}_{\Lambda\Lambda}$H+^{5}He+n(Q = 0.8MeV), ${}^{4}_{\Lambda\Lambda}$H+α+2n(Q = 1.6MeV) and ${}^{4}_{\Lambda\Lambda}$H +^{6} He(Q = 2.6MeV). A theory suggests a strong dependence of the production rate on the core structure [35]. The core of ${}^{10}_{\Lambda\Lambda}$Li* is ^{8}Li*, whose S^2 factor of ^{8}Li* $\rightarrow {}^{6}$ He + d is very large. It is likely that the $\Lambda\Lambda$ sticks to the deuteron and then ${}^{4}_{\Lambda\Lambda}$H is formed as "d+Λ+Λ". On the other hand, the final state, ${}^{7}_{\Lambda}$He+ ${}^{3}_{\Lambda}$H, is weakly produced in our data. Qualitatively speaking, if the mutual attraction between Λ's is attractive, $\Lambda\Lambda$ hypernuclei are more likely formed than twin single-Λ hypernuclei. The existence of the ${}^{4}_{\Lambda\Lambda}$H supports the attractive interaction of Λ-Λ, and gives a self-consistet picture.

5.4 Twin single hypernuclei, ${}^{4}_{\Lambda}$H and ${}^{3}_{\Lambda}$H

In the two dimensional plot (Fig 4.25), a large enhancement at 130$\leq P_{\pi 1} \leq$140 MeV/c and 110$\leq P_{\pi 2} \leq$120 MeV/c is observed. It is definitely the combination of ${}^{4}_{\Lambda}$H and ${}^{3}_{\Lambda}$H, twin single-Λ production. Because it is impossible to produce this via a stop-Ξ^- process due to the Q value, this is a clear evidence of twin single-Λ hypernuclear production via the direct process. This also gives good calibration points for the momentum in this region.

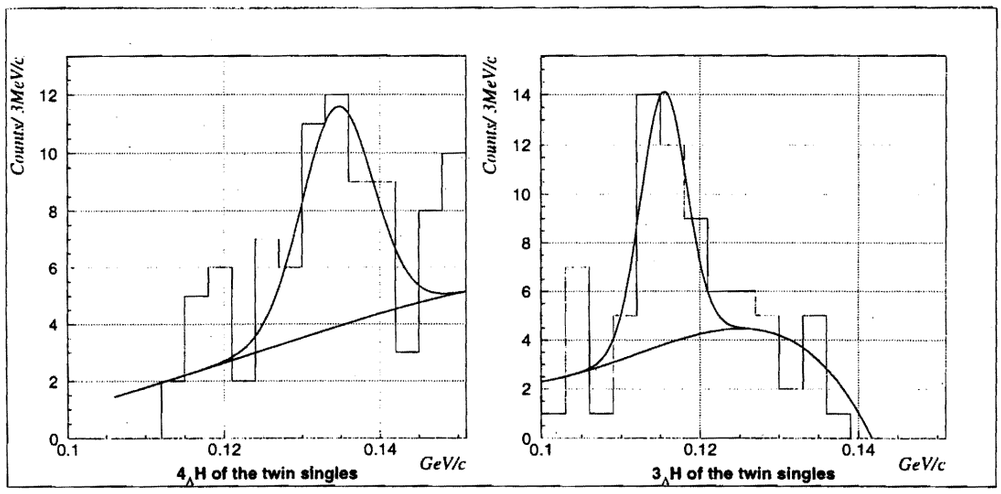

Figure 5.7: Projections of the momentum for twin hypernuclei, the left-hand side histogram shows the decay of ${}^{4}_{\Lambda}$H and the right-hand side histogram does that of ${}^{3}_{\Lambda}$H. The solid lines show the fitting result.

Fig 5.7 shows the projections of this enhancement onto $\pi 1$ and $\pi 2$ momentum axes. The left-hand side figure shows the projection of $\pi 1$ momentum, for which a fitting result with a Gaussian plus the background gives the peak position and the width in sigma to be 134.5$\pm$1.8 MeV/c and 4.6$\pm$2.2 MeV/c, respectively. Here the background means the Monte-Carlo simulation for the quasi-free Ξ^- decay described in subsection 4.3.2. The projection of $\pi 2$ momentum also gives the peak position and the width in sigma to be 115.4 $\pm$1.0 MeV/c and 2.9$\pm$0.9 MeV/c, respectively. In the Table 5.4, the fitting result is summarized. These peak positions are consistent with the well-known π^- momentum from ${}^{4}_{\Lambda}$H (132.9 MeV/c) and ${}^{3}_{\Lambda}$H (114.2 MeV/c) within a fitting error. The result of widths is also consistent with our estimation (4.79 MeV/c for ${}^{4}_{\Lambda}$H and 4.15 MeV/c for ${}^{3}_{\Lambda}$H, respectively).

Table 5.1: Summary of the fitting result for twin hypernuclei.

	$\pi 1$	$\pi 2$
Species	${}^{4}_{\Lambda}$H	${}^{3}_{\Lambda}$H
Centroid	134.5±1.8 MeV/c	115.4±1.0 MeV/c
Width	4.6±2.2 MeV/c	2.9±0.9 MeV/c

5.5 The other hypernuclei

Our histogram of two π^-'s shows not only the peaks studied in the last chapter but also some structure which might come from hypernuclei and others.

We can see a few counts around 130 MeV/c, where we expect the π^- from ${}^{5}_{\Lambda\Lambda}$H, but we need more statistics for a definite conclusion. We also search for the ${}^{6}_{\Lambda\Lambda}$He. ${}^{6}_{\Lambda\Lambda}$He decays into 3-body and the daughter nucleus also undergoes 3-body decay, ${}^{6}_{\Lambda\Lambda}\mathrm{He} \rightarrow {}^{5}_{\Lambda}\mathrm{He} + \mathrm{p} + \pi^-$ ~94 MeV/c, ${}^{5}_{\Lambda}He \rightarrow {}^{4}He + p + \pi^-$ 99 MeV/c. They appear in a low background region, so that we may get some information by a further analysis.

At last, the peak around 140 MeV/c is impressive , which shows a width of 7.3±2.8 MeV/c. It is hard to assign it as the π^- from any hypernuclei, because the highest π^- momentum from the hypernuclei is 132.9 MeV/c of ${}^{4}_{\Lambda}$H. The only one we can give an interpretation for is the π^- from stopped Ξ^-; $\Xi^- \rightarrow \Lambda + \pi^-$ (139 MeV/c). We suppose the π^- from the Ξ^- atom; Ξ^- decays via weak interaction in the atomic state before the $\Lambda\Lambda$ conversion reaction with the nuclei. If so, it is surprising to have such a long-lived atomic state even in a ^{9}Be target.

5.6 Background level

The normlization of the background level has been described in Section 4.3.2. For a further test of the absolute scale of the background, two $\pi 1$ histograms with the background curve are shown, to which the different cut conditions are applied.

Fig 5.8 shows the $\pi 1$ histogram without selecting the energy of Ξ^-, and Fig 5.9 shows the $\pi 1$ histogram with the cut condition that the polar angle of 2 π^- is larger than 60 degree. These two histograms also show the excess count only in the region less than 145 MeV/c as well as in Fig 4.26, even though the cut condition is different each other. This shows that the scale of the background level is normalized very well.

5.7 The future plan

Even though a complete performance could not be achieved due to the breakdown of the Z-chamber, we obtained a result concerning $\Lambda\Lambda$ hypernuclei by our CDS. We confirmed that our experimental method is feasible to search for S=-2 nuclear systems, including the $\Lambda\Lambda$ hypernuclei and so on. The detection of $\Lambda\Lambda$ hypernuclei

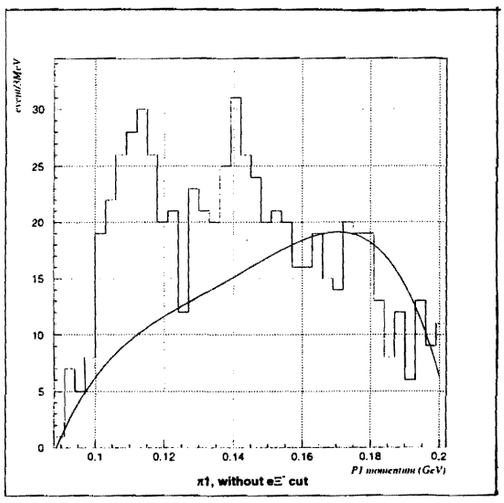

Figure 5.8: $\pi 1$ histogram without the cut condition that the energy of Ξ^- is less than 100 MeV.

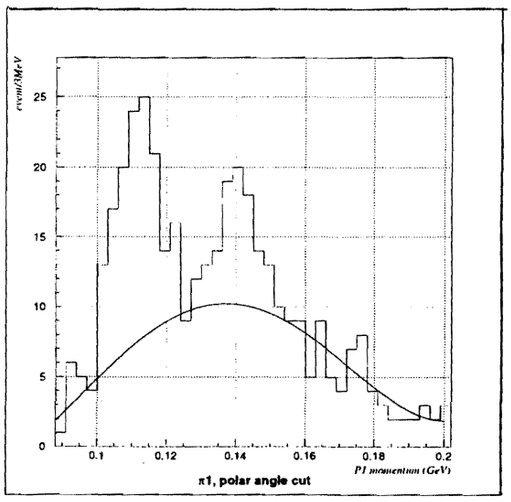

Figure 5.9: $\pi 1$ histogram with the cut condtion that the polar angle of two π^-'s is larger than 60 degrees.

is the most feasible way to measure the magnitude of the Λ-Λ interaction. In the future, the systematic study of the ΛΛ hypernuclei is expected and it will give us more precise information on Λ-Λ interaction. Some theorists claim an existence of "Hybrid H"; H particle in the nuclei [36]. Based on the accumulated data and more theoretial works, it will be clarified whether such an exotic nucleus exists or not.

Chapter 6

Conclusion

An experiment to search for the $\Lambda\Lambda$ hypernculei has been carried out. The experimental method for identifying $\Lambda\Lambda$ hypernuclei is based on the observation of the sequential decaying charged π^- from $\Lambda\Lambda$ hypernuclei in coincidence with the decaying π^- from single-Λ hypernuclei which are well known. This is the first time attempt to apply this method to detect the $\Lambda\Lambda$ hypernuclei. A Cylindrical Detector System(CDS) is constructed for this experiment. The CDS was optimized to detect decaying π^-'s from hypernuclei whose momenta are in the range 90~140 MeV/c , and the momentum resolution was finally achieved to be 8.2 MeV/c (FWHM) for 100 MeV/c.

In this thesis, the data collected during a run in 1998 is analyzed. We have approximately 1.1×10^5 Ξ^- which is clearly identified among $0.9\text{x}10^{12}$ incident kaons. Based on the 2 π^- events after the Ξ^- production and the background estimation, $\Lambda\Lambda$ hypernuclear formation has been searched for mainly in the slow-Ξ^- region. A Monte Carlo simulation has been done to estimate the background events mainly coming from the decay of quasi-free Ξ^-. The simulation can reproduce well the Ξ^- production via (K^-, K^+) reaction in our experimental condition. The excess counts over the estimated background have been observed, which are concentrated in the region where the decaying π^-'s from hypernuclei are expected, so that the production of the S=-2 nuclear system is inferred.

From detailed studies for the prominent structure in the region, where $\pi1$ momentum is between 110 and 125 MeV/c and $\pi2$ momentum is between 85 and 110 MeV/c, it was found that it is hard to understand the structure without assuming the sequential decay mode of ${}^{4}_{\Lambda\Lambda}\text{H} \rightarrow {}^{4}_{\Lambda}\text{He} + \pi^-$, ${}^{4}_{\Lambda}\text{He} \rightarrow {}^{3}\text{He} + \text{p} + \pi^-$and ${}^{4}_{\Lambda\Lambda}\text{H} \rightarrow {}^{3}_{\Lambda}\text{H} + \text{p} + \pi^-$, ${}^{3}_{\Lambda}\text{H} \rightarrow {}^{3}\text{He} + \pi^-$. We observed a peak in the $\pi1$ histogram with applying the cut condition; $\pi2$ momentum is between 85 and 100 MeV/c, which should enhance the π^- from ${}^{4}_{\Lambda\Lambda}\text{H}$. The peak gives the centroid and the width of 116.4±1.4(stat.)(MeV/c) and 4.6±1.7(MeV/c), respectively. Taking into account the error of momentum calibration as the systematic error, the peak position is 116.4±1.4(stat.)±1.2(syst.)(MeV/c). Assuming that the ${}^{4}_{\Lambda\Lambda}\text{H}$ mainly decays into the excited state of ${}^{4}_{\Lambda}\text{He}^*$(Ex=1.15(MeV)) due to the dominance of the spin non-flip amplitude in the pionic weak decay, this gives a ${}^{4}_{\Lambda\Lambda}\text{H}$ mass of 4106.2

± 0.94(stat.)± 0.80(syst.)(MeV), which corresponds to a $\Lambda\Lambda$ bond energy $\Delta B_{\Lambda\Lambda}$ of 0.47 ± 0.94(stat.)± 0.80(syst.)(MeV).

Our result gives a binding of ${}^{4}_{\Lambda\Lambda}\mathrm{H}$, by 0.6 MeV$\pm 0.94$(stat.)$\pm 0.80$(syst.). A theory, which can reproduce binding energies of ${}^{5}_{\Lambda}\mathrm{He}$, ${}^{9}_{\Lambda}\mathrm{Be}$ and ${}^{10}_{\Lambda\Lambda}\mathrm{Be}$, gives a prediction of the ${}^{4}_{\Lambda\Lambda}\mathrm{H}$ bound by 0.3 MeV below the ${}^{3}_{\Lambda}\mathrm{H} + \Lambda$ threshold. The theoretical prediction agrees with our result within the experimental error. In conclusion, the existence of ${}^{4}_{\Lambda\Lambda}\mathrm{H}$ supports an attractive interaction between Λ-Λ, and with constrains the effective Λ-Λ strength.

Acknowledgments

It's my great pleasure to express sincere thanks to many people for their collaboration, advice and encouragement during the work concerning BNL-AGS-E906 experiment. I also would like to acknowledge all the person who gave me the opportunities to work on the particle and nuclear physics.

First of all, I wish to express my thanks to my supervisor Prof. T. Fukuda, who is also the sporksman of E906 expriment. When I was at a loss the way to chose for the future, he introduced me to this kind of physics and gave me a chance of taking part in carring out an intriguing experiment and fabricating a fascinated experimental system. His flushes and extensive knowledge of nuclear physics inspire me in my years of graduated school.

I also would like to express special thanks to Prof. T. Nagae. He is a main planner of solenoid magnet. He gave me a lot of fruitful advice and insightful comments for my work. His objective view for my analysis made me be calm down so often. He instructs me in the essence of the experiment of nuclear physics.

I am grateful to Ms. M. Sekimoto for her assistance for fabricating the chamber. Her affection for the experimental hardware devices is the good example for me to follow.

I wish to express my thanks to T. Tamagawa. He played a mail role of the developing the HRM, which is the analyzing tool of CDS. His intensive work for the E906 led to the success of the experiment. He gave me the various discussion on the analysis method of the experiment and physics, which were very beneficial for me. He is also a best freiend of me.

I sincerely appreciate the great assistance of two physisists, Mr. H. Outa and Dr. S. Ajimura. It's very good experience for me to work with such experienced physisits. Mr. H. Outa joined to the preparation for the experiment and took shifts in BNL. He always attends to E906 meeting discussing data analysis twice a week and gave keen advices, which are very instructive for me. Dr. Ajimura give us his important time to prepare for and controll the physics run. His sharp perspection of experiment was very beneficial for me.

I greatly thank to Mr. V. Rasin, he helped me to fabricate the CDC and the Z-Chamber in Japan.

I greatly thank to Mr. H. Akikawa, he took a main role to oparate SSD system. Unfortunetely, SSD system did not work well because of hard air condition in experimental hall, but I honor his hard work. I also greatfully thanks to Dr. Y. Shimizu for planning the SSD system.

I would like to express special thanks to Prof. R. Chrien and Prof. M. Morgan, they gave me the chance of carring out the experiment in such a histric accelerator.

They gave me a productive discussion and valuable advice and supported me to accomplish the experiment.

Dr. A. Rusek, who has ability, agility and powerfullness, instructed me "How experimental physist should be in a battle-field". He gave me an enormous assitance and advice. Without him, we could not have lifted up our experiment safely. I sincerely thank to him.

I would like to express my sincere to technical staffs of medium energy, Mr. Edie. Myer oparated and maintained the beam line chamber, Mr. A. Minn prepared the equipments for the experiment, Mr. Rick Well fabricated a beutiful implementation for the CDS, and Mr. R. Sutter took part in planning and fabricating the electrical device and so on.

I am grateful to CMU memebers, Prof. Gregg B. Flankline, Prof. Reinhard Shumacher, Prof. Brian Quinn, Prof. Curtis Meyer, Dr. Alain Berdoz, Dr. Daniel Carman, Dr. Phil Koran, Dr. Kent Paschke, Dr P. Eugeno, Dr P. Khaustov, they are a part of original member established the D-line experimental hall. They supported not only to controlled DAQ system and 2nd lvl trigger system but also took shifts for a long period. I thank to Prof. B. Bassaleck, who is a member of D-line experiment from the first stage. I wish to thank to Dr. Jurgen Franz, Dr. H. Schmitt, they maintained the backward BD's chambers at 48D48 spectrometer system. I also thanks to Prof. Z. Meziani, he brought an Alpha computer for E906 analysis and took shifts. I also thanks to Dr. Michael Randry and Prof. Charles A. Davis from Uviversity of Manitoba, Dr. L. Gan and Dr. Yuan from Hampton University, A. Kurepin, M. Prokhvatilov and K. Shileev from INR (Moscow), they also took shifts in D-line. I also thank to Dr. H. Hotchi and Mr. K. Kubota from University of Tokyo, Dr. H. Khori from Osaka University and Ms. A. Ichikawa and Dr. J. K. Ahn from Kyoto University, they took "hard and cold" shift in D-line. They are E906 collaborators, whose productive discussion and valuable advice were so helpful for me.

I also thank to Mr. C. Pearson and technical staff in AGS. They appeard in D-line to oparate clane whenever we wanted. I thank to Prof. P. Pile, who is not only an AGS member but also a collaborator. He oparated the setting of upstream beam line to make good quality of K^- beam for E906. I sincerely thank to Prof. Rowenshtain and AGS administrators. They kept the AGS running and providing good quality beam.

I would like to express my special gratitude to Prof. T. Motoba and Prof. Y. Yamamoto, They gave me a lot of valuable advices and discussions about decay and formation of S=-2 nuclear systems. I also express my special thanks to Prof. Y. Akaishi, he gave us advices about their group's treatment of $\Lambda\Lambda$ interaction in ${}^{4}_{\Lambda\Lambda}$H. I also express my special thanks to Prof. Y. Yamada, his discussion about the formation probability of S=-2 system from ${}^{10}_{\Lambda\Lambda}$Li* is helpful for us to understand and classify the collected data.

I thank to other member of Fukuda group. Dr. Y. Mizoi gave me some good advice and discusstion about fabrication of the experimental devices are helpful for me. Mr. T. Miyach helped us to prepare the first physics run. I also would like to

express special thanks to members of PN-group of Kyoto University, Mr. K. Ozawa, Dr. H. Kanda, Dr. M. Ishino, Dr. S. Yokkaichi and Dr. S. Mihara. They not only lent me their DAQ system but also supported my experiment to test our CDC at KEK. They are my important friends, too. I thank to Mr. R. Sato and Mr. Saji from Osaka University, Mr. H. Torii from Kyoto University, they joined us to prepare for the test experiment at KEK. I also would like to thank to physicists, technical staffs and students of INS, they sometime gave me fruitful discussion or instruction, sometime assisted and encouraged me in my graduate school days. I especially thank to Prof. H. Hamagaki, his perspective view is very instructive for me and he accepts our favor to use the CPU cluster machine of his group for our data analysis.

I especially thanks to Ms. Cola Ferriciano, who is a secretary of medium energy group, I really appreciate her secretarial supports.

I wish to express my thanks to Non-chan, she always supports me. This thesis is dedecated to her. At last, I sincerely thank to my family. I couldn't have been finished this thesis without their great support. This thesis is also dedecated to the memory of my father, Shigeru Nakano.

Appendix A

The characteristic π^- momentum of hyperfragments from ${}^{10}_{\Lambda\Lambda}\mathrm{Li}^*$

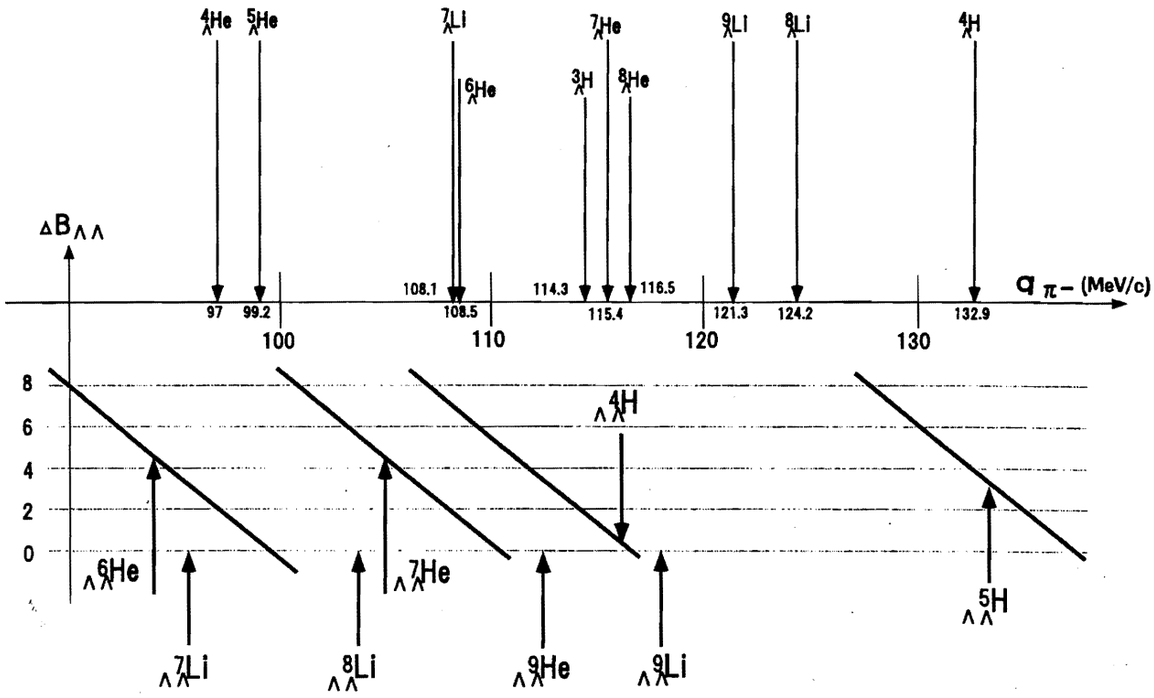

Figure A.1: The characteristic π^- momentum of hyperfragments from ${}^{10}_{\Lambda\Lambda}\mathrm{Li}^*$. Inclined lines show the relation between the bond energy of Λ-Λ in the $\Lambda\Lambda$ hypernuclei, $\Delta B_{\Lambda\Lambda}$, and the π^- momentum of the weak decay. The momenta of $\Lambda\Lambda$ hypernuclei indicated by arrows correspond to the theoretical predictions [31][32]. All, excepted for ${}^{4}_{\Lambda\Lambda}\mathrm{H}$, indicated the momentum to the ground state of the daughter nucleus, but some of them may favorably decay to the excited states.

List of Tables

List of Figures

Bibliography

[1] R. L. Jaffe, Phys. Rev. Lett. **38** (1997) 195.

[2] A. P. Balachandran, F. Lizzi, V. G. J. Rodgers, A. Stern, Nucl. Phys. **B256** (1985) 525.

[3] M. Oka, K. Shimizu, K. Yazaki, Nucl. Phys **A464** (1987) 700.

[4] U. Straub, Zong Ye Zhang, K. Bräuer, Amand Faessler, S.B. Khadkikar, Phys. Lett. **B200** (1988) 241.

[5] Y. Iwasaki,T. Yohsiè,Y. Tsuboi,Phys.Rev.Lett. **60** (1988) 1371.

[6] N. Kodama, M. Oka, T. Hatsuda et al., Nucl. Phys. **A580** (1994) 445.

[7] J. K. Ahn et al., Phys. Lett. **B444** (1998) 267.

[8] M. Danysz et al., Nucl. Phys. **49** (1963) 121.

[9] D.J. Prowse, Phys. Rev. Lett. **17** (1966) 782.

[10] S. Aoki et al., Prog. Theor. Phys. **85** (1991) 1287.

[11] R.H. Dalitz et al., Proc. R. Soc. Lond. **A426** (1989) 1-17.

[12] H. Bando, T. Motoba, J. Žofka, Int. J. Mod. Phys. **A5** (1990) 4021.

[13] C. B. Dover and A. Gal, Annals Phys. **146**, 309 (1983).

[14] J. Nakano, Master's thesis.

[15] T. Fukuda et al. (by KEK E224 group), Physical Review **C58** (1998) 1306.

[16] P. Khaustov, et al., Phys. Rev. **C61**, 054603(2000)

[17] K. Nakazawa, Proc. of the 23rd INS Int. Symp. on Nuclear and Particle Physics with Meson Beams in the 1 GeV/c Region, Tokyo, 1985, p.261.

[18] Y. Yamamoto, M. Wakai, T. Motoba and T. Fukuda, Nucl. Phys. **A625** (1997) 107.

[19] I. Kumagai-Fuse et al., Phys. Rev. **C54** (1996) 2843.

[20] T. Motoba, H. Bando, T. Fukuda, J. Zofka, Nucl. Phys. **A534** (1991) 597.

[21] Y. Akaishi and T. Yamazaki, Prog. Part. Nucle. Phys **39** (1997) 565.

[22] R.L. Gluckstern, Nucl. Instr. and Meth. 24, 381(1963).

[23] O. Nitoh,K. Takahashi,T. Shinohara,O. Tsumura and S. Uno, 'Drift Velocity of Electoron in Helium Based Gas Mixtures with a UV Laser'

[24] A. Peisert and F. Sauli: CERN 84-08 (1984)

[25] P. H. Pile et al., Nucl. Instr. Meth. **A321** (1992) 48.

[26] T. Iijima, Doctor thesis.

[27] V. Sum et al., Nucl. Instr. Meth. **A326** (1993) 489.

[28] E. Andersen et al., Nucl. Instr. Meth. **A320** (1992) 300.

[29] W. Blum, L. Rolandi and F.Bonaudi, Particle Detection with Drift Chamber, Springer-Verlag.

[30] S. Okabe and Y. Abe, Prog. Thero. Phys. **61** (1979) 1049: and private communication with Prof. S. Okabe.

[31] S. Nakaichi-Maeda and Y. Akaishi, Prog. Theor. Phys., **84** (1990) 1025.

[32] Y. Yamamoto, M. Wakai, T. Motoba and T. Fukuda. **A625** (1997) 107-142.

[33] Y. Akaishi, Nucl. Phys. **A547** (1992) 217c-226c.

[34] T. Motoba, private communication.

[35] Y. Yamada, private communication.

[36] A. R. Bodmer, Phys. Rev. **D4** (1971) 1601.